Assumed-modes modeling of piezoelectric energy harvesters: Euler–Bernoulli, Rayleigh, and Timoshenko models with axial deformations

Alper Erturk *

G. W. Woodruff School of Mechanical Engineering, Georgia Institute of Technology, Atlanta, GA 30332-0405, USA

ABSTRACT

A generalized framework is presented for the electromechanical modeling of base-excited piezoelectric energy harvesters with symmetric and unsymmetric laminates. The electromechanical derivations are given using the assumed-modes method under the Euler–Bernoulli, Rayleigh, and Timoshenko beam assumptions in three sections. The formulations account for an independent axial displacement variable and its electromechanical coupling in all cases. Comparisons are provided against the analytical solution for symmetric laminates and convergence of the assumed-modes solution to the analytical solution with increasing number of modes is shown. Model validations are also presented by comparing the electromechanical frequency response functions derived herein with the experimentally obtained ones in the absence and presence of a tip mass attachment. A discussion is provided for combination of the assumed-modes solution with nonlinear energy harvesting and storage circuitry. The electromechanical assumed-modes formulations can be used for modeling of piezoelectric energy harvesters with moderate thickness as well as those with unsymmetric laminates and varying geometry in the axial direction.

© 2012 Elsevier Ltd. All rights reserved.

1. Introduction

Vibration-based energy harvesting has received growing attention over the last decade. The goal in this research field is to power small electronic components by using the vibrational energy available in their environment so that the need for battery replacement and disposal can be minimized. Among the basic transduction mechanisms that can be used for converting ambient vibrations into electricity (electromagnetic [1–3], electrostatic [4–6], and piezoelectric [7–10] transduction techniques), piezoelectric transduction has been most heavily researched as summarized in several review articles [11–14] directly focusing on piezoelectric energy harvesting. The main advantages of piezoelectric materials over the other alternatives are their high power density, ease of application, and relative ease of fabrication at small scales [15,16]. Moreover, no bias voltage input is required (unlike the case of electrostatic transduction) and usable voltage levels can be obtained directly from the material itself without step-up conversion (unlike in electromagnetic induction).

Unless it is used as a surface patch [17], a cymbal [18] or a stack [19] configuration, typically, a piezoelectric energy harvester is a cantilevered beam with one or two piezoceramic layers

(a *unimorph* or a *bimorph*)[1] and it is located on a vibrating host structure for electrical power generation from bending vibrations [7–10]. The existing mechanics-based models mostly cover Euler–Bernoulli type formulation for thin beams with symmetric laminates. For symmetric and thin bimorph configurations, duToit et al. [8] and Elvin and Elvin [9] presented Rayleigh–Ritz type reduced-order solutions while Erturk and Inman [10] presented analytical solutions. The literature of energy harvesting lacks extensive treatment of unsymmetric laminates as well as generalized modeling of both thin and moderately thick configurations with varying geometric and material properties in a unified framework. Accurate reduced-order modeling of piezoelectric power generators is important not only for mechanical design (to tune the generator in order to match the fundamental resonance frequency with the

---

* Tel.: +1 404 385 1394; fax: +1 404 894 8496.
  E-mail address: alper.erturk@me.gatech.edu

[1] A review of unimorph and bimorph configurations as well as the associated modeling efforts until the early 1990s was presented as a part of an article by Smits and Choi [20] with a focus on sensing and actuation. In the 1990s, the application of piezoelectric materials for vibration damping [21,22] and shape control [23,24] in flexible structures received tremendous attention. Starting with the early 2000s to date, the use of structures with piezoelectric ceramics (the so-called piezoelectric energy harvesters) for converting ambient vibrations into electricity has become arguably the most heavily researched [11–14] application field of piezoelectric materials. The fields of shunt damping [21,22] and energy harvesting [11–14] are particularly related. Energy harvesting results in the shunt damping effect [25] (on the elastic generator itself) due to power transfer from the mechanical to electrical domain.

excitation frequency) but also to use the reduced-order electromechanical parameters in conjunction with nonlinear storage and impedance matching circuits [26–29] for system-level design and time-domain simulations. Considering that some of the recently proposed applications of piezoelectric energy harvesting aim to be a part of existing structural components for multifunctionality (such as the self-charging structure concept [30] that uses piezoelectric laminates along with thin-film batteries in wing spars of unmanned aerial vehicles [31]), it is required to extend the thin-beam derivations to moderately thick-beam configurations as well as varying geometries.

It is known from the literature of beam vibrations [32,33] that the dynamics of a beam-like structure strongly depends on its aspect ratio and the frequency range of interest. Moreover, laminated composite cantilevers may result in coupling between the transverse and longitudinal displacement components depending on the laminate characteristics [34] unlike a perfectly symmetric bimorph [10]. Han et al. [35] reviewed the Euler–Bernoulli model, the Rayleigh model, the shear model (which should not be confused with the *pure* shear beam model [36] that neglects the bending moment), and the Timoshenko model in a comparative study and presented frequency equations for different boundary conditions. The Euler–Bernoulli model is the classical beam model for slender beam configurations with sufficiently high length-to-thickness aspect ratio so that the shear distortion and rotary inertia effects are negligible. The Rayleigh model introduces the effect of rotary inertia to the Euler–Bernoulli model but it neglects the effect of transverse shear distortion. The shear model adds the effect of shear distortion to the Euler–Bernoulli model while neglecting the rotary inertia effect. The Timoshenko model accounts for both the shear distortion and rotary inertia effects and is widely used for modeling the dynamics of moderate length-to-thickness ratio beams for the first few vibration modes.

This paper presents approximate analytical distributed-parameter electromechanical modeling of cantilevered piezoelectric energy harvesters based on the Euler–Bernoulli, Rayleigh, and Timoshenko beam theories. The technique used here is an electromechanical version of the assumed-modes method [33], which is based on the extended Hamilton's principle for electromechanical media. After deriving the distributed-parameter energy expressions, the extended Hamilton's principle is employed to obtain the discretized electromechanical Lagrange's equations. An axial displacement variable is kept in the formulation to account for its coupling with the transverse displacement (in the Euler–Bernoulli and Rayleigh models) or cross-section rotation (in the Timoshenko model) due to possible structural asymmetry. The steady-state electromechanical response expressions are obtained for harmonic base excitation. Experimental validations are given for the thin-beam case by comparing the assumed-modes predictions with the experimental and analytical results for different number of modes in the absence and presence of a tip mass. The combined use the assumed-modes solution with nonlinear energy harvesting circuits is also discussed through the modally decoupled multi-mode transformer representation.

2. Electromechanical assumed-modes formulation of piezoelectric energy harvesters

2.1. Unimorph piezoelectric energy harvester and modeling assumptions

Consider the cantilevered piezoelectric energy harvester configuration shown in Fig. 1. The configuration has a single piezoceramic layer bonded onto a substructure layer and it is often called a *unimorph* cantilever. The perfectly conductive electrode pair of
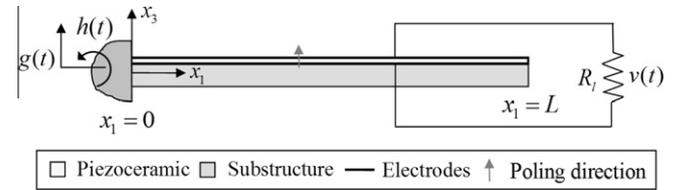

Fig. 1. Unimorph piezoelectric energy harvester with varying cross-section.

negligible thickness fully covers the upper and the lower faces of the piezoceramic layer separately and is connected to an external resistive electrical load. The layers are perfectly bonded to each other so there is no relative sliding at the interface. Deformations are assumed to be small and the material behavior is assumed to be linear so that the material, geometric, and dissipative nonlinearities [37,38] are not pronounced. The substructure layer is isotropic and the piezoceramic layer is transversely isotropic as it is poled in the thickness direction. The longitudinal axis is denoted by x_1 whereas the transverse axis is x_3 so that the neutral surface is coincident with the $x_1 x_2$-plane in the undeformed configuration. The goal is to express the voltage output across the external load in terms of the imposed base excitation.

The following Euler–Bernoulli, Rayleigh, and Timoshenko type derivations incorporate the modeling of energy harvester beams with varying cross-section and changing material properties in the x_1-direction as long as the cross-section is symmetric with respect to the $x_1 x_3$-plane. The coupling between the axial and transverse displacement components due to a possible structural asymmetry in the laminates is taken into consideration in all cases. The cantilever shown in Fig. 1 has no tip mass and the effect of a tip mass (with its mass moment of inertia) on the following formulation is discussed in Section 5 after the fundamental derivations.

As done in the analytical solutions for symmetric bimorph configurations given by Erturk and Inman [10], the base motion is represented as translation in the transverse direction with superimposed small rotation following Timoshenko et al. [32]. Therefore, the effective base displacement acting on the harvester structure is

$$w_b(x_1, t) = g(t) + x_1 h(t) \tag{1}$$

where $g(t)$ is the translation in the transverse direction and $h(t)$ is the superimposed small rotation.

2.2. Extended Hamilton's principle with electromechanical coupling

The extended Hamilton's principle with the internal electrical energy component is

$$\int_{t_1}^{t_2} (\delta T - \delta U + \delta W_{ie} + \delta W_{nc}) \mathrm{d}t = 0 \tag{2}$$

where δT, δU, δW_{ie}, and δW_{nc} are the first variations [39,40] of the total kinetic energy, the total potential energy, the internal electrical energy, and the work done by the non-conservative mechanical force and electric charge components. Eq. (2) is the electromechanical version of the Hamilton's principle that can be found in fundamental texts on analytical dynamics or vibrations [33].

In the formulation given here, the effect of base excitation is considered in the total kinetic energy term and the mechanical damping effect will be introduced later to the discretized equations. Hence the only non-conservative work in Eq. (2) is due to the electric charge output (Q) flowing to the external resistor such that $\delta W_{nc} = Q\delta v$, where v is the electric potential difference (i.e., voltage) across the resistive load, which will be the respective generalized coordinate.

The total potential energy in the structure is

$$U = \frac{1}{2}\left(\int_{V_s} \mathbf{S}^t \mathbf{T} dV_s + \int_{V_p} \mathbf{S}^t \mathbf{T} dV_p \right) \tag{3}$$

where $\mathbf{S}$ is the vector of engineering strain components, $\mathbf{T}$ is the vector of engineering stress components, the subscripts s and p stand for substructure and piezoceramic, respectively, the integrations are performed over the volume (V) of the respective material and the superscript t stands for transpose (otherwise it stands for time throughout the text).

The total kinetic energy of the system can be given by

$$T = \frac{1}{2}\left(\int_{V_s} \rho_s \frac{\partial \tilde{\mathbf{u}}^t}{\partial t} \frac{\partial \tilde{\mathbf{u}}}{\partial t} dV_s + \int_{V_p} \rho_p \frac{\partial \tilde{\mathbf{u}}^t}{\partial t} \frac{\partial \tilde{\mathbf{u}}}{\partial t} dV_p \right) \tag{4}$$

where ρ_s and ρ_p are the mass densities of the substructure and piezoceramic layers while $\tilde{\mathbf{u}}$ is the modified displacement vector that is the superposition of the effective base displacement input given by Eq. (1) and the displacement vector $\mathbf{u}$ defined with respect to the *moving* reference frame located at the clamped end[2]:

$$\tilde{\mathbf{u}} = \mathbf{u} + \{ 0 \quad 0 \quad w_b(x_1, t) \}^t \tag{5}$$

The internal electrical energy in the piezoceramic layer is

$$W_{ie} = \frac{1}{2} \int_{V_p} \mathbf{E}^t \mathbf{D} dV_p \tag{6}$$

where $\mathbf{E}$ is the vector of electric field components and $\mathbf{D}$ is the vector of electric displacement components.

2.3. Electromechanical Lagrange's equations based on the extended Hamilton's principle

The total kinetic energy, the total potential energy, and the internal electrical energy can be given in terms of the generalized coordinates as

$$T = T(q_1, q_2, \ldots, q_n, \dot{q}_1, \dot{q}_2, \ldots, \dot{q}_n),$$
$$U = U(q_1, q_2, \ldots, q_n), \quad W_{ie} = W_{ie}(q_1, q_2, \ldots, q_n) \tag{7}$$

where the over-dots represent differentiation with respect to time. Here, one of the generalized coordinates is the electrical across variable, i.e., the *voltage* across the load. Note that the alternative approach is to use the *electric charge* as the generalized coordinate as in the basic derivations of Crandall et al. [40] and it can be shown through Legendre transformation that the same equations would be obtained (since the energy and co-energy components are identical for the static capacitance of the linear system).

The first variations of the foregoing expressions are

$$\delta T = \sum_{k=1}^n \left(\frac{\partial T}{\partial q_k} \delta q_k + \frac{\partial T}{\partial \dot{q}_k} \delta \dot{q}_k \right), \quad \delta U = \sum_{k=1}^n \frac{\partial U}{\partial q_k} \delta q_k,$$
$$\delta W_{ie} = \sum_{k=1}^n \frac{\partial W_{ie}}{\partial q_k} \delta q_k \tag{8}$$

and the virtual work done by the generalized non-conservative forces (Q_k) is then

$$\delta W_{nc} = \sum_{k=1}^n Q_k \delta q_k \tag{9}$$

Substituting Eqs. (8) and (9) into Eq. (2) and integrating by parts gives

$$\int_{t_1}^{t_2} \left\{ \sum_{k=1}^n \left[\frac{\partial T}{\partial q_k} - \frac{\partial U}{\partial q_k} + \frac{\partial W_{ie}}{\partial q_k} + Q_k - \frac{d}{dt}\left(\frac{\partial T}{\partial \dot{q}_k} \right) \right] \delta q_k \right\} dt = 0 \tag{10}$$

Based on the standard argument that the extended Hamilton's principle must hold for arbitrary and independent virtual displacements, Eq. (10) leads to the electromechanical Lagrange's equations:

$$\frac{d}{dt}\left(\frac{\partial T}{\partial \dot{q}_k} \right) - \frac{\partial T}{\partial q_k} + \frac{\partial U}{\partial q_k} - \frac{\partial W_{ie}}{\partial q_k} = Q_k \tag{11}$$

where the dissipative effects can be represented as generalized non-conservative terms.

2.4. Electromechanical Euler–Bernoulli model with axial deformations

The displacement field in the Euler–Bernoulli model is

$$\mathbf{u} = \left\{ u_1^0(x_1, t) - x_3 \frac{\partial u_3^0(x_1, t)}{\partial x_1} \quad 0 \quad u_3^0(x_1, t) \right\}^t \tag{12}$$

where $u_1^0(x_1, t)$ and $u_3^0(x_1, t)$ are the axial displacement and the transverse displacement of the neutral surface at point x_1 and time t relative to the moving base. From this displacement field, the only non-zero strain component can be extracted as

$$S_1 = \frac{\partial u_1^0}{\partial x_1} - x_3 \frac{\partial^2 u_3^0}{\partial x_1^2} \tag{13}$$

The isotropic substructure obeys Hooke's law:

$$T_1 = Y_s S_1 \tag{14}$$

where Y_s is the elastic modulus of the substructure layer. Here and hereafter, the contracted notation (i.e., Voigt's notation: $11 \to 1$, $22 \to 2$, $33 \to 3$, $23 \to 4$, $13 \to 5$, $12 \to 6$) is directly used in the subscripts.

The constitutive equations for the stress and the electric displacement components in the piezoceramic layers are

$$T_1 = \bar{c}_{11}^E S_1 - \bar{e}_{31} E_3 = \bar{c}_{11}^E \left(\frac{\partial u_1^0}{\partial x_1} - x_3 \frac{\partial^2 u_3^0}{\partial x_1^2} \right) + \bar{e}_{31} \frac{v}{h_p} \tag{15}$$

$$D_3 = \bar{e}_{31} S_1 + \bar{\varepsilon}_{33}^S E_3 = \bar{e}_{31} \left(\frac{\partial u_1^0}{\partial x_1} - x_3 \frac{\partial^2 u_3^0}{\partial x_1^2} \right) - \bar{\varepsilon}_{33}^S \frac{v}{h_p} \tag{16}$$

where $\bar{c}_{11}^E$ is the elastic modulus of the piezoceramic layer at constant electric field, $\bar{e}_{31}$ is the effective piezoelectric stress constant, $\bar{\varepsilon}_{33}^S$ is the permittivity component at constant strain (see Appendix A.1 for these reduced terms), E_3 is the electric field component, and D_3 is the electric displacement component in the x_3-direction (i.e., the *poling* direction). Since $E_i = -\partial\varphi/\partial x_i$ for an electric potential φ, the electric field in Eqs. (15) and (16) is directly expressed in terms of the voltage across the external load as $E_3 = -v/h_p$, where h_p is the thickness of the piezoceramic layer.

The distributed-parameter variables in the mechanical domain are $u_3^0(x_1, t)$ and $u_1^0(x_1, t)$ whereas the electrical variable is $v(t)$. The following two finite series represent the two components of the vibration response:

$$u_3^0(x_1, t) = \sum_{r=1}^N a_r(t)\phi_r(x_1), \quad u_1^0(x_1, t) = \sum_{r=1}^N b_r(t)\alpha_r(x_1) \tag{17}$$

where $\phi_r(x_1)$ and $\alpha_r(x_1)$ are the kinematically admissible trial functions which satisfy the respective essential boundary conditions while $a_r(t)$ and $b_r(t)$ are the unknown generalized coordinates. For notation simplicity, the same number of modes (N) is used in Eq. (17), which is not a necessary condition, i.e., different number of modes can associate with different generalized coordinates.

---

[2] Alternatively, one could express the total kinetic energy relative to the moving base and include the work done by the base excitation as a non-conservative effect.

Following the derivation given in Section 2.3, the electromechanical Lagrange's equations for the Euler–Bernoulli model are obtained based on the extended Hamilton's principle as

$$\mathbf{m^{aa}\ddot{a}} - \mathbf{m^{ab}\ddot{b}} + \mathbf{d^{aa}\dot{a}} - \mathbf{d^{ab}\dot{b}} + \mathbf{k^{aa}a} - \mathbf{k^{ab}b} - \boldsymbol{\theta^a}\, v = \mathbf{f} \tag{18}$$

$$-\mathbf{m^{ab}\ddot{a}} + \mathbf{m^{bb}\ddot{b}} - \mathbf{d^{ab}\dot{a}} + \mathbf{d^{bb}\dot{b}} - \mathbf{k^{ab}a} + \mathbf{k^{bb}b} + \boldsymbol{\theta^b}\, v = \mathbf{0} \tag{19}$$

$$C_p \dot{v} + \frac{v}{R_l} + (\boldsymbol{\theta^a})^t \dot{\mathbf{a}} - (\boldsymbol{\theta^b})^t \dot{\mathbf{b}} = 0 \tag{20}$$

Here, $\mathbf{a} = \{a_1 \quad a_2 \quad \ldots \quad a_N\}^t$, $\mathbf{b} = \{b_1 \quad b_2 \quad \ldots \quad b_N\}^t$, $\boldsymbol{\theta^a} = \{\theta_1^a \quad \theta_2^a \quad \ldots \quad \theta_N^a\}^t$, $\boldsymbol{\theta^b} = \{\theta_1^b \quad \theta_2^b \quad \ldots \quad \theta_N^b\}^t$, $\mathbf{f} = \{f_1 \quad f_2 \quad \ldots \quad f_N\}^t$ (where f_i emerges from $\partial T/\partial \dot{a}_i$), and C_p is the capacitance of the piezoceramic layer given by $C_p = \bar{\varepsilon}_{33}^S A_e/h_p$ (where A_e is the electrode area) while the matrix and vector components are

$$m_{rl}^{aa} = \int_0^L (\rho_s A_s + \rho_p A_p)\phi_r(x_1)\phi_l(x_1)\mathrm{d}x_1 \tag{21}$$

$$m_{rl}^{bb} = \int_0^L (\rho_s A_s + \rho_p A_p)\alpha_r(x_1)\alpha_l(x_1)\mathrm{d}x_1 \tag{22}$$

$$m_{rl}^{ab} = \int_0^L (\rho_s H_s + \rho_p H_p)\phi_r'(x_1)\alpha_l(x_1)\mathrm{d}x_1 \tag{23}$$

$$k_{rl}^{aa} = \int_0^L (Y_s I_s + \bar{c}_{11}^E I_p)\phi_r''(x_1)\phi_l''(x_1)\mathrm{d}x_1 \tag{24}$$

$$k_{rl}^{bb} = \int_0^L (Y_s I_s + \bar{c}_{11}^E I_p)\alpha_r'(x_1)\alpha_l'(x_1)\mathrm{d}x_1 \tag{25}$$

$$k_{rl}^{ab} = \int_0^L (Y_s H_s + \bar{c}_{11}^E H_p)\phi_r''(x_1)\alpha_l'(x_1)\mathrm{d}x_1 \tag{26}$$

$$\theta_r^a = \int_0^L J_p \phi_r''(x_1)\mathrm{d}x_1 \tag{27}$$

$$\theta_r^b = \int_0^L B_p \alpha_r'(x_1)\mathrm{d}x_1 \tag{28}$$

$$f_r = -\frac{\mathrm{d}^2 g(t)}{\mathrm{d}t^2}\int_0^L (\rho_s A_s + \rho_p A_p)\phi_r(x_1)\mathrm{d}x_1$$
$$-\frac{\mathrm{d}^2 h(t)}{\mathrm{d}t^2}\int_0^L (\rho_s A_s + \rho_p A_p)x_1\phi_r(x_1)\mathrm{d}x_1 \tag{29}$$

where $r = 1, \ldots, N$ and $l = 1, \ldots, N$, the primes represent differentiation with respect to the space variable x_1, and the following area moments and coupling terms are defined for convenience:

$$\{A_s, H_s, I_s\} = \int\int_s \{1, x_3, x_3^2\}\mathrm{d}x_2\mathrm{d}x_3 \tag{30}$$

$$\{A_p, H_p, I_p\} = \int\int_p \{1, x_3, x_3^2\}\mathrm{d}x_2\mathrm{d}x_3 \tag{31}$$

$$B_p = \int\int_p \frac{\bar{e}_{31}}{h_p}\mathrm{d}x_2\mathrm{d}x_3 \tag{32}$$

$$J_p = \int\int_p \frac{\bar{e}_{31}}{h_p}x_3\mathrm{d}x_2\mathrm{d}x_3 \tag{33}$$

In Eqs. (18) and (19), the damping matrix $\mathbf{d}$ accounts for the mechanical dissipation effects and it is assumed to be linearly proportional to the mass and the stiffness matrices (Rayleigh damping [41]) so that the system under short-circuit or open-circuit conditions is a normal mode system:

$$\begin{bmatrix} \mathbf{d^{aa}} & -\mathbf{d^{ab}} \\ -\mathbf{d^{ab}} & \mathbf{d^{bb}} \end{bmatrix} = \mu \begin{bmatrix} \mathbf{m^{aa}} & -\mathbf{m^{ab}} \\ -\mathbf{m^{ab}} & \mathbf{m^{bb}} \end{bmatrix} + \gamma \begin{bmatrix} \mathbf{k^{aa}} & -\mathbf{k^{ab}} \\ -\mathbf{k^{ab}} & \mathbf{k^{bb}} \end{bmatrix} \tag{34}$$

where μ and γ are the real constants of mass and stiffness proportionality, respectively.

2.5. Electromechanical Rayleigh model with axial deformations

The displacement field in the Rayleigh model is identical to the form given by Eq. (12). The only difference is that the rotary inertia effect is taken into consideration in the Rayleigh model. Therefore, as compared to the Euler–Bernoulli model given in Section 2.4, the difference is due to the submatrix m_{rl}^{aa}, which takes the following form instead of Eq. (21):

$$m_{rl}^{aa} = \int_0^L \left[(\rho_s A_s + \rho_p A_p)\phi_r(x_1)\phi_l(x_1) + (\rho_s I_s + \rho_p I_p)\phi_r'(x_1)\phi_l'(x_1)\right]\mathrm{d}x_1 \tag{35}$$

The governing electromechanical equations have the form of Eqs. (18)–(20). The form of Eqs. (22)–(29) remain the same as they are not affected by the distributed rotary inertia of the harvester beam.

2.6. Electromechanical Timoshenko model with axial deformations

The displacement field in the Timoshenko formulation is

$$\mathbf{u} = \left\{ u_1^0(x_1, t) - x_3\psi^0(x_1, t) \quad 0 \quad u_3^0(x_1, t) \right\}^t \tag{36}$$

where $u_1^0(x_1, t)$ and $u_3^0(x_1, t)$ are the axial displacement and the transverse displacement of the neutral surface at point x_1 and time t relative to the moving base and $\psi^0(x_1, t)$ is the cross-section rotation.

The two non-zero strain components obtained from the given displacement field are

$$S_1 = \frac{\partial u_1^0}{\partial x_1} - x_3\frac{\partial \psi^0}{\partial x_1} \tag{37}$$

$$S_5 = \frac{\partial}{\partial x_3}(u_1^0 - x_3\psi^0) + \frac{\partial u_3^0}{\partial x_1} = \frac{\partial u_3^0}{\partial x_1} - \psi^0 \tag{38}$$

where S_1 is the axial strain component and S_5 is the transverse engineering shear strain component.

The isotropic substructure has the following constitutive equations:

$$T_1 = Y_s S_1 = Y_s\left(\frac{\partial u_1^0}{\partial x_1} - x_3\frac{\partial \psi^0}{\partial x_1}\right) \tag{39}$$

$$T_5 = \kappa G_s S_5 = \kappa G_s\left(\frac{\partial u_3^0}{\partial x_1} - \psi^0\right) \tag{40}$$

where κ is Timoshenko's cross-section dependent shear correction factor [42,43] and it accounts for the non-uniform distribution of shear stresses over the cross-section.[3] Furthermore, G_s is the shear modulus of the substructure layer and it is related to the elastic modulus of the substructure layer through

$$G_s = \frac{Y_s}{2(1 + v_s)} \tag{41}$$

where v_s is the Poisson's ratio of the substructure layer.

The constitutive equations for the piezoceramic layer can be given by

---

[3] Various expressions [42–52] have been derived for the shear correction factor since Timoshenko's beam theory [42] was established. A review of the shear correction factors proposed in 1921–1975 was presented by Kaneko [47], concluding that the expressions derived by Timoshenko [43] should be preferred. For rectangular cross-sections, Timoshenko [43] derived $\kappa = (5 + 5v)/(6 + 5v)$ (where is the Poisson's ratio for the beam material) theoretically whereas Mindlin [44,45] obtained $\kappa = \pi^2/12$ experimentally for crystal plates. Cowper's [46] solution is also widely used and it differs slightly from Timoshenko's solution: $\kappa = (10 + 10v)/(12 + 11v)$. The effect of width-to-depth ratio of the cross-section has been taken into account by Stephen [48,49] and more recently by Hutchinson [50,51]. Recently, an experimental study on the effect of width-to-depth ratio of the cross-section has been presented by Puchegger et al. [52].

$$T_1 = \bar{c}_{11}^E S_1 - \bar{e}_{31} E_3 = \bar{c}_{11}^E \left(\frac{\partial u_1^0}{\partial x_1} - x_3 \frac{\partial \psi^0}{\partial x_1} \right) + \bar{e}_{31} \frac{v}{h_p} \tag{42}$$

$$T_5 = \kappa \bar{c}_{55}^E S_5 = \kappa \bar{c}_{55}^E \left(\frac{\partial u_3^0}{\partial x_1} - \psi^0 \right) \tag{43}$$

$$D_3 = \bar{e}_{31} S_1 + \bar{\varepsilon}_{33}^S E_3 = \bar{e}_{31} \left(\frac{\partial u_1^0}{\partial x_1} - x_3 \frac{\partial \psi^0}{\partial x_1} \right) - \bar{\varepsilon}_{33}^S \frac{v}{h_p} \tag{44}$$

where, in particular, $\bar{c}_{55}^E$ is the effective shear modulus of the piezoceramic layer at constant electric field and the expressions for these reduced terms are given in Appendix A.2.

The distributed-parameter variables in the mechanical domain are $u_3^0(x_1, t)$, $u_1^0(x_1, t)$, and $\psi^0(x_1, t)$ while the electrical variable is $v(t)$. The following finite series represent the components of vibration response:

$$u_3^0(x_1, t) = \sum_{r=1}^{N} a_r(t) \phi_r(x_1),$$

$$u_1^0(x_1, t) = \sum_{r=1}^{N} b_r(t) \alpha_r(x_1), \quad \psi^0(x_1, t) = \sum_{r=1}^{N} c_r(t) \beta_r(x_1) \tag{45}$$

Then the electromechanical Lagrange's equations for the Timoshenko model are obtained as

$$\mathbf{m^{aa}\ddot{a} + d^{aa}\dot{a} - d^{ac}\dot{c} + k^{aa}a - k^{ac}c = f} \tag{46}$$

$$\mathbf{m^{bb}\ddot{b} - m^{bc}\ddot{c} + d^{bb}\dot{b} - d^{bc}\dot{c} + k^{bb}b - k^{bc}c + \theta^b \, v = 0} \tag{47}$$

$$\mathbf{-m^{bc}\ddot{b} + m^{cc}\ddot{c} - d^{ac}\dot{a} - d^{bc}\dot{b} + d^{cc}\dot{c} - k^{ac}a - k^{bc}b + k^{cc}c - \theta^c \, v = 0} \tag{48}$$

$$C_p \dot{v} + \frac{v}{R_l} - (\theta^b)^t \dot{\mathbf{b}} + (\theta^c)^t \dot{\mathbf{c}} = 0 \tag{49}$$

Here, $\mathbf{a} = \{a_1 \ a_2 \ \dots \ a_N\}^t$, $\mathbf{b} = \{b_1 \ b_2 \ \dots \ b_N\}^t$, $\mathbf{c} = \{c_1 \ c_2 \ \dots \ c_N\}^t$, $\boldsymbol{\theta}^\mathbf{b} = \{\theta_1^b \ \theta_2^b \ \dots \ \theta_N^b\}^t$, $\boldsymbol{\theta}^\mathbf{c} = \{\theta_1^c \ \theta_2^c \ \dots \theta_N^c\}^t$, and $\mathbf{f} = \{f_1 \ f_2 \ \dots \ f_N\}^t$ (where f_i is again due to $\partial T / \partial \dot{a}_i$), while the matrix and vector components are

$$m_{rl}^{aa} = \int_0^L (\rho_s A_s + \rho_p A_p) \phi_r(x_1) \phi_l(x_1) dx_1 \tag{50}$$

$$m_{rl}^{bb} = \int_0^L (\rho_s A_s + \rho_p A_p) \alpha_r(x_1) \alpha_l(x_1) dx_1 \tag{51}$$

$$m_{rl}^{cc} = \int_0^L (\rho_s I_s + \rho_p I_p) \beta_r(x_1) \beta_l(x_1) dx_1 \tag{52}$$

$$m_{rl}^{bc} = \int_0^L (\rho_s H_s + \rho_p H_p) \alpha_r(x_1) \beta_l(x_1) dx_1 \tag{53}$$

$$k_{rl}^{aa} = \int_0^L \kappa (G_s A_s + \bar{c}_{55}^E A_p) \phi_r'(x_1) \phi_l'(x_1) dx_1 \tag{54}$$

$$k_{rl}^{bb} = \int_0^L (Y_s A_s + \bar{c}_{11}^E A_p) \alpha_r'(x_1) \alpha_l'(x_1) dx_1 \tag{55}$$

$$k_{rl}^{cc} = \int_0^L \left[(Y_s I_s + \bar{c}_{11}^E I_p) \beta_r'(x_1) \beta_l'(x_1) + \kappa (G_s A_s + \bar{c}_{55}^E A_p) \beta_r(x_1) \beta_l(x_1) \right] dx_1 \tag{56}$$

$$k_{rl}^{ac} = \int_0^L \kappa (G_s A_s + \bar{c}_{55}^E A_p) \phi_r'(x_1) \beta_l(x_1) dx_1 \tag{57}$$

$$k_{rl}^{bc} = \int_0^L (Y_s H_s + \bar{c}_{11}^E H_p) \alpha_r'(x_1) \beta_l'(x_1) dx_1 \tag{58}$$

$$\theta_r^b = \int_0^L B_p \alpha_r'(x_1) dx_1 \tag{59}$$

$$\theta_r^c = \int_0^L J_p \beta_r'(x_1) dx_1 \tag{60}$$

$$f_r = -\frac{d^2 g(t)}{dt^2} \int_0^L (\rho_s A_s + \rho_p A_p) \phi_r(x_1) dx_1 - \frac{d^2 h(t)}{dt^2}$$

$$\int_0^L (\rho_s A_s + \rho_p A_p) x_1 \phi_r(x_1) dx_1 \tag{61}$$

where $r = 1, \dots, N$ and $l = 1, \dots, N$. Rayleigh damping is assumed to account for the mechanical dissipation effects, where the damping matrix $\mathbf{d}$ is given as a linear combination of the mass and the stiffness matrices through the real constants of proportionality μ and γ:

$$\begin{bmatrix} \mathbf{d^{aa}} & \mathbf{0} & -\mathbf{d^{ac}} \\ \mathbf{0} & \mathbf{d^{bb}} & -\mathbf{d^{bc}} \\ -\mathbf{d^{ac}} & -\mathbf{d^{bc}} & \mathbf{d^{cc}} \end{bmatrix} = \mu \begin{bmatrix} \mathbf{m^{aa}} & \mathbf{0} & \mathbf{0} \\ \mathbf{0} & \mathbf{m^{bb}} & -\mathbf{m^{bc}} \\ \mathbf{0} & -\mathbf{m^{bc}} & \mathbf{m^{cc}} \end{bmatrix}$$
$$+ \gamma \begin{bmatrix} \mathbf{k^{aa}} & \mathbf{0} & -\mathbf{k^{ac}} \\ \mathbf{0} & \mathbf{k^{bb}} & -\mathbf{k^{bc}} \\ -\mathbf{k^{ac}} & -\mathbf{k^{bc}} & \mathbf{k^{cc}} \end{bmatrix} \tag{62}$$

3. Solution of the governing electromechanical equations

The governing equations in the previous sections given by Eqs. (18)–(20) for the Euler–Bernoulli and Rayleigh models and by Eqs. (46)–(49) for the Timoshenko model can easily be put into the first-order form in order to handle arbitrary base translation and small rotation inputs by numerical solution given the initial conditions. For the special case of harmonic base excitation, this section presents closed-form expressions for the electromechanically coupled vibration and electrical response at steady state.

3.1. Euler–Bernoulli and Rayleigh models

If the base displacement components are harmonic of the forms $g(t) = W_0 \, e^{j\omega t}$ and $h(t) = \vartheta_0 e^{j\omega t}$ (where ω is the excitation frequency and j is the unit imaginary number), then the forcing vector given by Eq. (29) becomes

$$\mathbf{f} = \mathbf{F} e^{j\omega t} \tag{63}$$

where

$$F_r = \sigma_r \omega^2 W_0 \int_0^L (\rho_s A_s + \rho_p A_p) \phi_r(x) dx + \tau_r \omega^2 \vartheta_0 \int_0^L (\rho_s A_s + \rho_p A_p) x \phi_r(x) dx \tag{64}$$

Based on the linear system assumption, the generalized coordinates in the response expansions given by Eq. (17) are also harmonic of the form $\mathbf{a} = \mathbf{A} e^{j\omega t}$ and $\mathbf{b} = \mathbf{B} \, e^{j\omega t}$ while $v = V e^{j\omega t}$ at steady state. After substituting these response forms into Eqs. (18)–(20) and performing matrix manipulations, one can obtain the steady-state response for the voltage across the load and the vibration response components as

$$v(t) = j\omega \left(j\omega C_p + \frac{1}{R_l} \right)^{-1} \left[-(\theta^\mathbf{a})^t + (\theta^\mathbf{b})^t (\Gamma^\mathbf{bb})^{-1} \Gamma^\mathbf{ba} \right]$$
$$\times [\Gamma^\mathbf{aa} - \Gamma^\mathbf{ab} (\Gamma^\mathbf{bb})^{-1} \Gamma^\mathbf{ba}]^{-1} \mathbf{F} e^{j\omega t} \tag{65}$$

$$u_3^0(x_1, t) = \mathbf{\Phi}^t(x_1) [\Gamma^\mathbf{aa} - \Gamma^\mathbf{ab} (\Gamma^\mathbf{bb})^{-1} \Gamma^\mathbf{ba}]^{-1} \mathbf{F} e^{j\omega t} \tag{66}$$

$$u_1^0(x_1, t) = \boldsymbol{\alpha}^t(x_1) (\Gamma^\mathbf{bb})^{-1} \Gamma^\mathbf{ba} [\Gamma^\mathbf{aa} - \Gamma^\mathbf{ab} (\Gamma^\mathbf{bb})^{-1} \Gamma^\mathbf{ba}]^{-1} \mathbf{F} e^{j\omega t} \tag{67}$$

where $\mathbf{\Phi}(x_1)$ and $\boldsymbol{\alpha}(x_1)$ the vectorial representations of the respective admissible function sets $\phi_r(x_1)$ and $\alpha_r(x_1)$ in Eq. (17) while the remaining terms are

$$\Gamma^\mathbf{aa} = -\omega^2 \mathbf{m^{aa}} + j\omega \mathbf{d^{aa}} + \mathbf{k^{aa}} + j\omega \left(j\omega C_p + \frac{1}{R_l} \right)^{-1} \theta^\mathbf{a} (\theta^\mathbf{a})^t \tag{68}$$

$$\Gamma^\mathbf{bb} = -\omega^2 \mathbf{m^{bb}} + j\omega \mathbf{d^{bb}} + \mathbf{k^{bb}} + j\omega \left(j\omega C_p + \frac{1}{R_l} \right)^{-1} \theta^\mathbf{b} (\theta^\mathbf{b})^t \tag{69}$$

$$\Gamma^\mathbf{ab} = -\omega^2 \mathbf{m^{ab}} + j\omega \mathbf{d^{ab}} + \mathbf{k^{ab}} + j\omega \left(j\omega C_p + \frac{1}{R_l} \right)^{-1} \theta^\mathbf{a} (\theta^\mathbf{b})^t \tag{70}$$

$$\Gamma^\mathbf{ba} = -\omega^2 \mathbf{m^{ab}} + j\omega \mathbf{d^{ab}} + \mathbf{k^{ab}} + j\omega \left(j\omega C_p + \frac{1}{R_l} \right)^{-1} \theta^\mathbf{b} (\theta^\mathbf{a})^t \tag{71}$$

Here, the relevant matrices and vectors are due to Eqs. (21)–(29) and (34) for the Euler–Bernoulli model while Eq. (35) replaces Eq. (21) for the Rayleigh model.

3.2. Timoshenko model

Assuming the harmonic forms $g(t) = W_0 e^{j\omega t}$ and $h(t) = \vartheta_0 e^{j\omega t}$ for the base motion input, the forcing vector again takes the form given by Eq. (63). Then the generalized coordinates in Eq. (45) take the steady-state forms of $\mathbf{a} = \mathbf{A}e^{j\omega t}$, $\mathbf{b} = \mathbf{B}\,e^{j\omega t}$, and $\mathbf{c} = \mathbf{C}e^{j\omega t}$, while the steady-state voltage output becomes $v = Ve^{j\omega t}$. These response forms can be substituted into Eqs. (46)–(49) to obtain

$$v(t) = j\omega \left(j\omega C_p + \frac{1}{R_l} \right)^{-1} \left[(\tilde{\theta}^{\mathbf{b}})^t (\mathbf{\Gamma}^{\mathbf{bb}})^{-1} \mathbf{\Gamma}^{\mathbf{bc}} - (\tilde{\theta}^{\mathbf{c}})^t \right] \{ \mathbf{\Gamma}^{\mathbf{aa}} (\mathbf{\Gamma}^{\mathbf{ca}})^{-1} [\mathbf{\Gamma}^{\mathbf{cc}} \\ - \mathbf{\Gamma}^{\mathbf{cb}} (\mathbf{\Gamma}^{\mathbf{bb}})^{-1} \mathbf{\Gamma}^{\mathbf{bc}}] - \mathbf{\Gamma}^{\mathbf{ac}} \}^{-1} \mathbf{F} e^{j\omega t} \tag{72}$$

$$u_3^0(x_1, t) = \mathbf{\Phi}^t(x_1) (\mathbf{\Gamma}^{\mathbf{ca}})^{-1} [\mathbf{\Gamma}^{\mathbf{cc}} - \mathbf{\Gamma}^{\mathbf{cb}} (\mathbf{\Gamma}^{\mathbf{bb}})^{-1} \mathbf{\Gamma}^{\mathbf{bc}}] \{ \mathbf{\Gamma}^{\mathbf{aa}} (\mathbf{\Gamma}^{\mathbf{ca}})^{-1} [\mathbf{\Gamma}^{\mathbf{cc}} \\ - \mathbf{\Gamma}^{\mathbf{cb}} (\mathbf{\Gamma}^{\mathbf{bb}})^{-1} \mathbf{\Gamma}^{\mathbf{bc}}] - \mathbf{\Gamma}^{\mathbf{ac}} \}^{-1} \mathbf{F} e^{j\omega t} \tag{73}$$

$$u_1^0(x_1, t) = \boldsymbol{\alpha}^t(x_1) (\mathbf{\Gamma}^{\mathbf{bb}})^{-1} \mathbf{\Gamma}^{\mathbf{bc}} \{ \mathbf{\Gamma}^{\mathbf{aa}} (\mathbf{\Gamma}^{\mathbf{ca}})^{-1} [\mathbf{\Gamma}^{\mathbf{cc}} - \mathbf{\Gamma}^{\mathbf{cb}} (\mathbf{\Gamma}^{\mathbf{bb}})^{-1} \mathbf{\Gamma}^{\mathbf{bc}}] \\ - \mathbf{\Gamma}^{\mathbf{ac}} \}^{-1} \mathbf{F} e^{j\omega t} \tag{74}$$

$$\psi^0(x_1, t) = \boldsymbol{\beta}^t(x_1) \{ \mathbf{\Gamma}^{\mathbf{aa}} (\mathbf{\Gamma}^{\mathbf{ca}})^{-1} [\mathbf{\Gamma}^{\mathbf{cc}} - \mathbf{\Gamma}^{\mathbf{cb}} (\mathbf{\Gamma}^{\mathbf{bb}})^{-1} \mathbf{\Gamma}^{\mathbf{bc}}] \\ - \mathbf{\Gamma}^{\mathbf{ac}} \}^{-1} \mathbf{F} e^{j\omega t} \tag{75}$$

where $\mathbf{\Phi}(x_1)$, $\boldsymbol{\alpha}(x_1)$, and $\boldsymbol{\beta}(x_1)$ are the vectorial representations of the respective admissible function sets $\phi_r(x_1)$, $\alpha_r(x_1)$, and $\beta_r(x_1)$ in Eq. (45) while the remaining terms are

$$\mathbf{\Gamma}^{\mathbf{aa}} = -\omega^2 \mathbf{m}^{\mathbf{aa}} + j\omega \mathbf{d}^{\mathbf{aa}} + \mathbf{k}^{\mathbf{aa}} \tag{76}$$

$$\mathbf{\Gamma}^{\mathbf{bb}} = -\omega^2 \mathbf{m}^{\mathbf{bb}} + j\omega \mathbf{d}^{\mathbf{bb}} + \mathbf{k}^{\mathbf{bb}} + j\omega \left(j\omega C_p + \frac{1}{R_l} \right)^{-1} \theta^{\mathbf{b}} (\theta^{\mathbf{b}})^t \tag{77}$$

$$\mathbf{\Gamma}^{\mathbf{cc}} = -\omega^2 \mathbf{m}^{\mathbf{cc}} + j\omega \mathbf{d}^{\mathbf{cc}} + \mathbf{k}^{\mathbf{cc}} + j\omega \left(j\omega C_p + \frac{1}{R_l} \right)^{-1} \theta^{\mathbf{c}} (\theta^{\mathbf{c}})^t \tag{78}$$

$$\mathbf{\Gamma}^{\mathbf{ac}} = \mathbf{\Gamma}^{\mathbf{ca}} = j\omega \mathbf{d}^{\mathbf{ac}} + \mathbf{k}^{\mathbf{ac}} \tag{79}$$

$$\mathbf{\Gamma}^{\mathbf{bc}} = -\omega^2 \mathbf{m}^{\mathbf{bc}} + j\omega \mathbf{d}^{\mathbf{bc}} + \mathbf{k}^{\mathbf{bc}} + j\omega \left(j\omega C_p + \frac{1}{R_l} \right)^{-1} \theta^{\mathbf{b}} (\theta^{\mathbf{c}})^t \tag{80}$$

$$\mathbf{\Gamma}^{\mathbf{cb}} = -\omega^2 \mathbf{m}^{\mathbf{bc}} + j\omega \mathbf{d}^{\mathbf{bc}} + \mathbf{k}^{\mathbf{bc}} + j\omega \left(j\omega C_p + \frac{1}{R_l} \right)^{-1} \theta^{\mathbf{c}} (\theta^{\mathbf{b}})^t \tag{81}$$

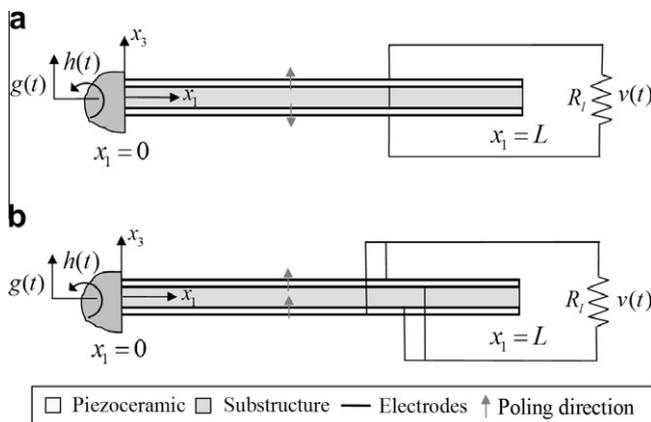and the relevant matrices and vectors are due to Eqs. (50)–(62).

Fig. 2. Bimorph piezoelectric energy harvester configurations with symmetric laminates and varying cross-section: (a) series connection and (b) parallel connection.

4. Modeling of configurations with symmetric laminates: Bimorph configurations

4.1. Euler–Bernoulli and Rayleigh models

For a geometrically symmetric configuration (i.e., configuration with symmetric laminates with respect to the neutral surface) such as the bimorph cantilevers [10] shown in Fig. 2, the H_s and H_p terms causing the coupling between the transverse displacement and the axial displacement vanish, reducing the discretized equations of the system given by Eqs. (18)–(20) to

$$\mathbf{m}^{\mathbf{aa}} \ddot{\mathbf{a}} + \mathbf{d}^{\mathbf{aa}} \dot{\mathbf{a}} + \mathbf{k}^{\mathbf{aa}} \mathbf{a} - \theta^{\mathbf{a}} v = \mathbf{f} \tag{82}$$

$$C_p^{eq} \dot{v} + \frac{v}{R_l} + (\theta^{\mathbf{a}})^t \dot{\mathbf{a}} = 0 \tag{83}$$

This simplest form is similar to the symmetric thin bimorph equations derived using the Rayleigh–Ritz method [8,9]. The capacitance term here for the case of multiple piezoelectric laminates is the equivalent capacitance C_p^{eq} (which depends on the way the electrode pairs are combined, e.g., series or parallel as in Fig. 2). Likewise the coupling vector ($\theta^{\mathbf{a}}$) depends on the way the electrode pairs are connected. Table 1 summarizes the equivalent capacitance and electromechanical coupling terms for symmetric bimorph configurations modeled based on the Euler–Bernoulli and Rayleigh beam theories.

4.2. Timoshenko model

For a geometrically symmetric cantilever, Eq. (47) decouples from the electromechanical equations of the system, yielding

$$\mathbf{m}^{\mathbf{aa}} \ddot{\mathbf{a}} + \mathbf{d}^{\mathbf{aa}} \dot{\mathbf{a}} - \mathbf{d}^{\mathbf{ac}} \dot{\mathbf{c}} + \mathbf{k}^{\mathbf{aa}} \mathbf{a} - \mathbf{k}^{\mathbf{ac}} \mathbf{c} = \mathbf{f} \tag{84}$$

$$\mathbf{m}^{\mathbf{cc}} \ddot{\mathbf{c}} - \mathbf{d}^{\mathbf{ac}} \dot{\mathbf{a}} + \mathbf{d}^{\mathbf{cc}} \dot{\mathbf{c}} - \mathbf{k}^{\mathbf{ac}} \mathbf{a} + \mathbf{k}^{\mathbf{cc}} \mathbf{c} - \theta^{\mathbf{c}} v = \mathbf{0} \tag{85}$$

$$C_p^{eq} \dot{v} + \frac{v}{R_l} + (\theta^{\mathbf{c}})^t \dot{\mathbf{c}} = 0 \tag{86}$$

where the capacitance $\left(C_p^{eq} \right)$ and the electromechanical coupling ($\theta^{\mathbf{c}}$) terms are again for the equivalent of multiple layers. For symmetric bimorph configurations modeled based on the Timoshenko beam theory, these terms are as given in Table 2.

5. Presence of a tip mass in the Euler–Bernoulli, Rayleigh, and Timoshenko models

If the energy harvester configuration shown in Fig. 1 has a tip mass of M_t with a mass moment of inertia of I_t attached rigidly at $x_1 = L$, the total kinetic energy expressions should be modified accordingly in the electromechanical models discussed in this paper. Such a modification in the total kinetic energy alters the mass matrices as well as the effective forcing term resulting from base excitation as summarized in the following. In the following discussion, the moment of inertia I_t of the tip mass accounts for its geometric information in case the point mass assumption fails (for a relatively large tip mass). Some authors prefer expanding the term I_t [53,54] whereas this compact representation is preferred here as in Erturk and Inman [10]. It is important to note that

Table 1
Equivalent capacitance and electromechanical coupling terms for bimorphs with symmetric laminates modeled based on the Euler–Bernoulli and Rayleigh beam theories.

	Series connection	Parallel connection
C_p^{eq}	$\bar{\varepsilon}_{33}^S A_e / 2h_p$	$2\bar{\varepsilon}_{33}^S A_e / h_p$
θ_r^a	$\int_0^L J_p \phi_r''(x_1) dx_1$	$2 \int_0^L J_p \phi_r''(x_1) dx_1$

Table 2
Equivalent capacitance and electromechanical coupling terms for bimorphs with symmetric laminates modeled based on the Timoshenko beam theory.

	Series connection	Parallel connection
C_p^{eq}	$\bar{\varepsilon}_{33}^S A_e / 2h_p$	$2\bar{\varepsilon}_{33}^S A_e / h_p$
θ_r^c	$\int_0^L J_p \beta_r'(x_1) dx_1$	$2\int_0^L J_p \beta_r'(x_1) dx_1$

I_t should be expressed at the end of the elastic point (on the neutral axis) where the boundary condition is written ($x_1 = L$), which requires using the parallel-axis theorem [55] to shift the centroidal mass moment of inertia to this point.

5.1. Euler–Bernoulli model

In the Euler–Bernoulli model, inclusion of a tip mass modifies the sub-matrix m_{rl}^{aa} to

$$m_{rl}^{aa} = \int_0^L (\rho_s A_s + \rho_p A_p)\phi_r(x_1)\phi_l(x_1)dx_1 + M_t\phi_r(L)\phi_l(L) + I_t\phi_r'(L)\phi_l'(L) \tag{87}$$

5.2. Rayleigh model

After the inclusion of the tip mass, the sub-matrix m_{rl}^{aa} in the Rayleigh model becomes

$$m_{rl}^{aa} = \int_0^L [(\rho_s A_s + \rho_p A_p)\phi_r(x_1)\phi_l(x_1) + (\rho_s I_s + \rho_p I_p)\phi_r'(x_1)\phi_l'(x_1)]dx_1 + M_t\phi_r(L)\phi_l(L) + I_t\phi_r'(L)\phi_l'(L) \tag{88}$$

5.3. Timoshenko model

The sub-matrices altered in the Timoshenko model due to this modification are m_{rl}^{aa} and m_{rl}^{cc}:

$$m_{rl}^{aa} = \int_0^L (\rho_s A_s + \rho_p A_p)\phi_r(x_1)\phi_l(x_1)dx_1 + M_t\phi_r(L)\phi_l(L) \tag{89}$$

$$m_{rl}^{cc} = \int_0^L (\rho_s I_s + \rho_p I_p)\beta_r(x_1)\beta_l(x_1)dx_1 + I_t\beta_r(L)\beta_l(L) \tag{90}$$

5.4. Modification of the effective force

In the Euler–Bernoulli, Rayleigh and Timoshenko models, the base excitation term f_r derived from the total kinetic energy expression becomes

$$f_r = -\frac{d^2 g(t)}{dt^2}\left[\int_0^L (\rho_s A_s + \rho_p A_p)\phi_r(x_1)dx_1 + M_t\phi_r(L)\right] - \frac{d^2 h(t)}{dt^2}\left[\int_0^L (\rho_s A_s + \rho_p A_p)x_1\phi_r(x_1)dx_1 + M_t L\phi_r(L)\right] \tag{91}$$

6. Comments on the kinematically admissible trial functions

6.1. Euler–Bernoulli and Rayleigh models

According to the kinematic boundary conditions at the clamped end, the admissible functions in Eq. (17) should satisfy

$$\phi_r(0) = 0, \quad \phi_r'(0) = 0, \quad \alpha_r(0) = 0 \tag{92}$$

For the admissible functions $\phi_r(x_1)$ of the transverse displacement, one can use the eigenfunctions of the respective symmetric structure [10] (Fig. 2). Therefore,

$$\phi_r(x_1) = \cos\frac{\lambda_r}{L}x_1 - \cosh\frac{\lambda_r}{L}x_1 + \frac{\sin\lambda_r - \sinh\lambda_r + \lambda_r\frac{M_t}{mL}(\cos\lambda_r - \cosh\lambda_r)}{\cos\lambda_r + \cosh\lambda_r - \lambda_r\frac{M_t}{mL}(\sin\lambda_r - \sinh\lambda_r)}\left(\sin\frac{\lambda_r}{L}x_1 - \sinh\frac{\lambda_r}{L}x_1\right) \tag{93}$$

Here, λ_r is the rth root of the transcendental equation

$$1 + \cos\lambda\cosh\lambda + \lambda\frac{M_t}{mL}(\cos\lambda\sinh\lambda - \sin\lambda\cosh\lambda) - \frac{\lambda^3 I_t}{mL^3}(\cosh\lambda\sin\lambda + \sinh\lambda\cos\lambda) + \frac{\lambda^4 M_t I_t}{m^2 L^4}(1 - \cos\lambda\cosh\lambda) = 0 \tag{94}$$

where m is the mass per length of the beam:

$$m = \rho_s A_s + \rho_p A_p \tag{95}$$

Eqs. (93) and (94) simplify dramatically in the absence of a tip mass ($M_t = I_t = 0$). In fact, even in the presence of a tip mass, one can use the simplified form of Eq. (93) with $M_t = 0$ which is still kinematically admissible for λ_r obtained from

$$1 + \cos\lambda\cosh\lambda = 0 \tag{96}$$

However, in the presence of a tip mass, using the eigenvalues obtained from Eq. (94) leads to faster convergence (with less number of modes) in the discretized system. Note that the foregoing admissible functions become the eigenfunctions for a thin (Euler–Bernoulli type) structure with symmetric laminates.

If one prefers to avoid the hyperbolic functions appearing in the eigenfunctions of the symmetric structure, the following is a typical admissible function used for clamped-free boundary conditions [56]:

$$\phi_r(x_1) = 1 - \cos\left[\frac{(2r-1)\pi x_1}{2L}\right] \tag{97}$$

which satisfies $\phi_r(0) = \phi_r'(0) = 0$. Polynomial forms and static solutions can also be used to satisfy $\phi_r(0) = \phi_r'(0) = 0$.

Similarly, the eigenfunctions of the symmetric structure under longitudinal vibrations [57] can be used as the admissible functions of the unsymmetric structure here:

$$\alpha_r(x_1) = \sin\frac{\eta_r}{L}x_1 \tag{98}$$

where η_r is the rth root of the transcendental equation

$$\frac{M_t}{mL}\eta_r\sin\eta_r - \cos\eta_r = 0 \tag{99}$$

Alternatively, the roots of $\cos\eta_r = 0$ (i.e. $\eta_r = (2r-1)\pi/2$, $r = 1, 2, \ldots, N$) can be used in Eq. (98) for simplicity.

6.2. Timoshenko model

Based on the kinematic boundary conditions at the clamped end, the admissible functions in Eq. (45) should satisfy

$$\phi_r(0) = 0, \quad \alpha_r(0) = 0, \quad \beta_r(0) = 0 \tag{100}$$

For $\phi_r(0) = 0$ to be satisfied, one can use the form of $\phi_r(x_1)$ given by Eq. (93). However, for this choice of $\phi_r(x_1)$, it is useful to note that $\phi_r'(0) = 0$ implies zero shear strain at the root (due to $\beta_r(0) = 0$), which is not realistic for a clamped boundary. A simple trigonometric function similar to Eq. (97) could be a better alternative compared to Eq. (93). Eqs. (100) also accept trigonometric forms. Alternatively, polynomial forms can be employed. Several other options exist in the literature to use as the trial functions for

Timoshenko beams, such as the implementations of Chebyshev polynomials [58] and static solutions [59].

7. Experimental validation for a brass-reinforced PZT-5H bimorph cantilever

7.1. Experimental setup

The cantilever used for model validation is a brass-reinforced bimorph (T226-H4–203X) manufactured by Piezo Systems Inc. As shown in Fig. 3, a small electromagnetic shaker (TMC Solution TJ-2) is used for base excitation of the bimorph cantilever and the acceleration at the base of the cantilever is measured by a small accelerometer (PCB Piezotronics U352C67) attached to the aluminum clamp of the cantilever using wax. The tip velocity of the cantilever in the transverse direction is measured using a laser vibrometer (Polytec PDV100) by attaching a small reflector tape at the tip of the cantilever. The data acquisition system (SigLab 20–42) receives three simultaneous measurements (base acceleration, voltage across the load, and tip velocity response) and processes these data to give the voltage output – to – base acceleration and the tip velocity – to – base acceleration frequency response functions (FRFs). Chirp excitation (burst type with five averages) is provided to the shaker from the output channel of the data acquisition system (which is connected to a Hewlett–Packard 6826A power supply before the electromagnetic shaker). Since the purpose is validating the linear electromechanical derivations, it is ensured that the base acceleration level in the FRF measurements is less than $0.1g$ so that the material, dissipative, and geometric nonlinearities [37,38] are not pronounced. This acceleration level sufficiently represents the level of vibration in various ambient vibrational energy sources as reviewed by Roundy et al. [60].

The bimorph cantilever is composed of two oppositely poled thin PZT-5H piezoelectric elements bracketing a brass substructure layer. The brass layer provides the electrical conductivity between the bottom electrode of the top layer and the top electrode of the bottom layer. Therefore, collecting the charge output from the outermost electrodes becomes the series connection case as in the schematic given by Fig. 2a. The geometric and the material properties of the piezoceramic and the substructure layers in the cantilevered condition are given in Table 3. Typical properties for PZT-5H [61] are used here to calculate the effective parameters (Appendix A.1). Note that, in agreement with the formulation, the length is the overhang length of the harvester, i.e. it is not the total free length (31.8 mm) of the bimorph as received from the manufacturer. The overhang length of the cantilever is measured as 24.53 mm. A reflector tape of negligible mass is attached close to the tip of the beam and the position of velocity measurement on the reflector is approximately 1.5 mm from the free end ($x_1 = 23$ mm is used in the tip deflection calculation). The set of resistors used in the experiment ranges from 470 Ω to 995 kΩ.
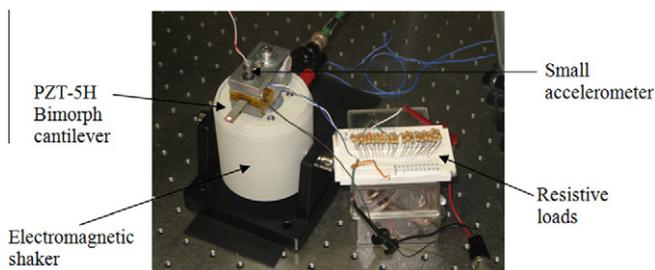

Fig. 3. Experimental setup showing the brass-reinforced PZT-5H bimorph cantilever clamped to the armature of a shaker and a set of resistive loads.

Table 3
Geometric and material properties of the PZT-5H bimorph cantilever.

	Piezoceramic (PZT-5H)	Substructure (brass)
Length [mm]	24.53	24.53
Width [mm]	6.4	6.4
Thickness [mm]	0.265 (each)	0.140
Mass density [kg/m³]	7500	9000
Elastic modulus [GPa]	60.6	105
Effective piezoelectric constant [C/m²]	−16.6	–
Permittivity constant [nF/m]	25.55	–

The 12 resistors used in the experiment sufficiently represent the range between the short-circuit and open-circuit conditions.

The sample used in the experiments is thin enough to neglect the effects of shear distortion and rotary inertia in modeling for the fundamental vibration mode. Hence, the Euler–Bernoulli type assumed-modes formulation (Section 2.5) is employed in the model simulations. According to the geometric and materials properties of the cantilever given in Table 3, the coupling between the independent transverse and longitudinal displacement components vanishes (Section 4.1). The admissible function used in all simulations is the trigonometric admissible function given by Eq. (97). All comparisons are given against the experimental measurements as well as the formerly presented analytical solution [10]. The purely mechanical viscous damping ratio (ζ) is identified as 0.874% for the fundamental vibration mode from the first FRF measurement, i.e., $\zeta_1 = 0.00874$ [63].

7.2. Electromechanical FRFs and model validation

Fig. 4 shows the assumed-modes predictions of the electromechanical FRFs for all resistors with only one mode used in the solution ($N = 1$). Note that the base acceleration in both FRFs is normalized with respect to the gravitational acceleration, $g = 9.81$ m/s², and the arrows in each set of FRFs indicate the direction of increasing load resistance. Both the voltage and the tip velocity predictions are highly inaccurate especially in terms of the resonance frequency when $N = 1$. If the number of modes in the assumed-modes solution is increased to $N = 3$, the predictions are improved substantially as observed in Fig. 5 (see also Table 4). The resonance frequencies shown in Table 4 are the fundamental short-circuit ($R_l \rightarrow 0$) and open-circuit ($R_l \rightarrow \infty$) resonance frequencies. Further increase in the number of modes up to $N = 5$ (Fig. 6) and then to $N = 10$ (Fig. 7) provides uniform convergence to the analytical [10] frequencies (Table 4). Although increasing the number of modes any further does not seem to be improving the model predictions considerably, including more modes improve the predictions of higher vibration modes which are not discussed here. Note that, the fundamental natural frequency estimated using this technique gives an upper bound for the lowest natural frequency [33] (as in the Rayleigh–Ritz method); that is, the approximated fundamental natural frequency cannot underestimate the analytical value regardless of the number of modes used. The reader is referred to Meirovitch [33] for an extensive discussion on the Rayleigh–Ritz and assumed-modes methods, their differences, and relations to the analytical solution for conventional (passive) vibrating systems. If the exact eigenfunctions are used in the solution (which are available in this case due to Eq. (93)), using only one mode is sufficient for practical purposes and the results become identical to the predictions of the single-mode analytical solution [10].

Further discussion of practical value is related to the variations of the electrical and mechanical response amplitudes (per base
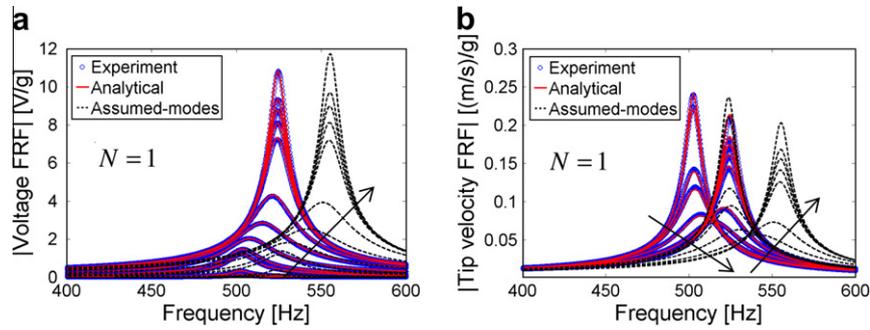
Fig. 4. Comparison of the (a) voltage FRFs and (b) tip velocity FRFs against the experimental data and the analytical solution (N = 1 in the assumed-modes solution and the arrows indicate the direction of increasing load resistance).
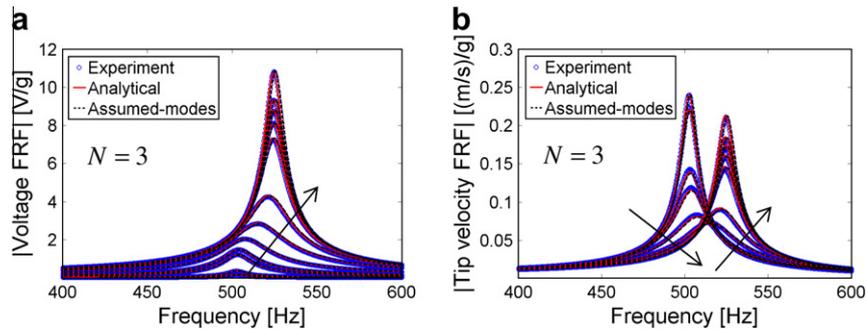

Fig. 5. Comparison of the (a) voltage FRFs and (b) tip velocity FRFs against the experimental data and the analytical solution (N = 3 in the assumed-modes solution and the arrows indicate the direction of increasing load resistance).

acceleration) with changing load resistance at the fundamental short-circuit and open-circuit resonance frequencies, 502.6 Hz and 524.5 Hz, respectively. The variation of the voltage output is shown in Fig. 8a, where the voltage amplitude increases monotonically with increasing load resistance at both frequencies. The opposite but still monotonic behavior is observed in the current versus load resistance diagram shown in Fig. 8b. In both cases, excitation at the short-circuit resonance frequency gives larger output when the system is close to short-circuit conditions, and vice versa for the open-circuit resonance frequency. The most important output in energy harvesting is the electrical power, which is illustrated in Fig. 8c. Since the system is lightly damped and strongly coupled [62,63], approximately the same power output (0.22 mW/g^2) is delivered to substantially different optimal resistance values (7.6 kΩ at 502.6 Hz and 189 kΩ at 524.5 Hz). The effect of Joule heating in the resistor [22,25] on the dynamics of the generator can be found in Fig. 8d, which displays the tip velocity versus load resistance curves at these two frequencies. Significant vibration attenuation is observed in Fig. 8d in the region of maximum power transfer to the electrical load. It is important to note that the velocity response measured by the laser vibrometer is the *absolute* velocity response relative to the fixed reference frame (superposition of the base motion and the relative vibratory motion, analogous to Eq. (5)).

7.3. Effect of a tip mass on the frequency response

In order to investigate the effect of a tip mass and to demonstrate the validity of the model in the presence of a tip mass, a cube-shaped rectangular mass is attached to the tip of the brass-reinforced PZT-5H bimorph cantilever tested here (Fig. 9a). The tip mass information is introduced to the model directly and the accuracy of the model predictions is checked without changing

the overhang length of the beam as well as the clamping condition. At tip of the cantilever, the mass moment of inertia about the center axis of the bimorph is obtained from

$$I_t = M_t \left[\frac{a^2}{6} + \left(\frac{a + h_s}{2} + h_p \right)^2 \right] \tag{101}$$

where $M_t = 0.239 \times 10^{-3}$ kg (measured), the first term inside the parenthesis is for the mass moment of inertia about the center axis of the cube and the second term is due to the parallel-axis theorem [55] to account for the offset of the tip mass to one side (the geometric parameters can be found in Fig. 9b, where a = 3.2 mm). Substituting the numerical data into Eq. (101), the mass moment of inertia at the tip of the cantilever is calculated as $I_t = 1.285 \times 10^{-9}$ kg.m^2. The purely mechanical viscous damping ratio for the fundamental vibration mode is identified as 0.845% from the first FRF measurement.

Table 4
Assumed-modes predictions of the fundamental short-circuit and open-circuit resonance frequencies of the voltage FRF (compared against the analytical and the experimental results).

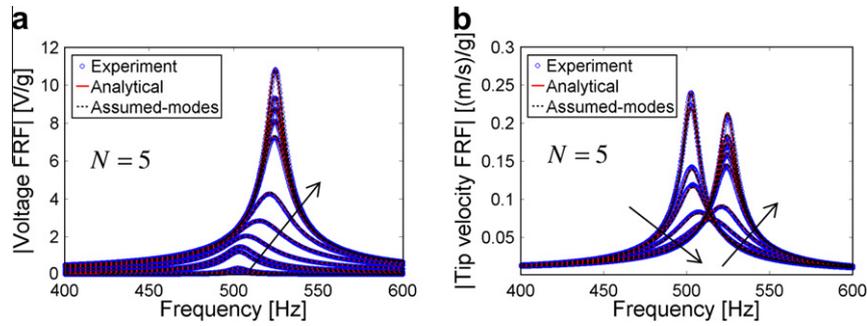|	Short-circuit resonance frequency [Hz]	Open-circuit resonance frequency [Hz]
Experimental	502.5	524.7
Analytical	502.6	524.5
Assumed-modes (N = 1)	523.8	555.3
Assumed-modes (N = 3)	503.2	525.5
Assumed-modes (N = 5)	502.7	524.7
Assumed-modes (N = 10)	502.6	524.5

Fig. 6. Comparison of the (a) voltage FRFs and (b) tip velocity FRFs against the experimental data and the analytical solution ($N = 5$ in the assumed-modes solution and the arrows indicate the direction of increasing load resistance).
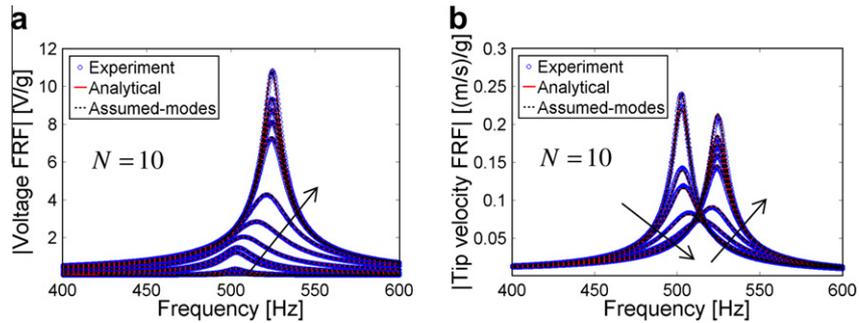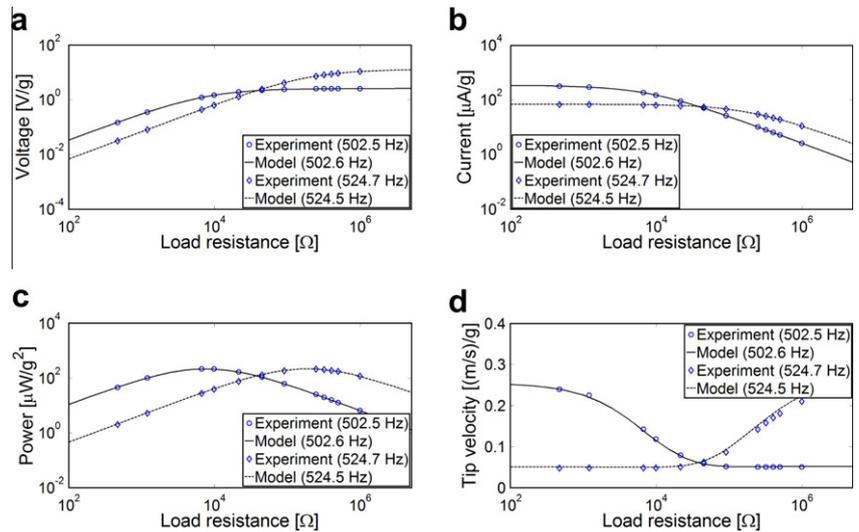

Fig. 7. Comparison of the (a) voltage FRFs and (b) tip velocity FRFs against the experimental data and the analytical solution ($N = 10$ in the assumed-modes solution and the arrows indicate the direction of increasing load resistance).

Fig. 8. Variations of the (a) voltage, (b) current, (c) power, and (d) tip velocity amplitudes (per base acceleration input) with changing load resistance for excitations at the fundamental short-circuit and open-circuit resonance frequencies ($N = 10$).

After employing the tip mass information in the assumed-modes model, a similar convergence investigation can be performed as done in the absence of a tip mass (Figs. 4–7). Here, only the final electromechanical FRFs for $N = 10$ (10 modes used in the solution) are shown in Fig. 10 while the fundamental short-circuit and open-circuit frequencies for different number of modes are summarized in Table 5. As in the previous case (no tip mass), these frequencies are identical to those obtained from the analytical solution [10] when $N = 10$ is used in the assumed-modes solution.

For excitations at the fundamental short-circuit and open-circuit resonance frequencies, the performance diagrams shown in Fig. 11 exhibit similar characteristics to those given by Fig. 8 (in the absence of a tip mass). However, it is important to note that the response amplitudes have increased as compared to the case without a tip mass. Particularly, the maximum power output for excitations at the fundamental short-circuit or open-circuit resonance frequencies (338.5 Hz and 355.4 Hz, respectively) is now 0.46 mW/g² (which is twice the power output normalized with
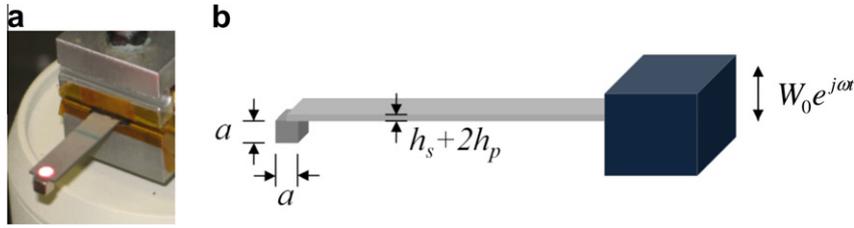
Fig. 9. Bimorph cantilever after the addition of the cube-shaped tip mass: (a) close-up view and (b) schematic.

respect to base acceleration amplitude as compared to the previous case).

8. On the dynamics of combined power generator – energy storage systems

8.1. The concept of combining a reduced-order transformer model with nonlinear circuitry

In addition to the fact that the assumed-modes formulations given here incorporate structural configurations with changing geometric and material properties as well as unsymmetric and moderately thick laminates, an important practical use is its ease of implementation to combine with circuit simulation software for predicting the system dynamics in the presence of sophisticated storage electronics that require time-domain numerical simulations. This approach follows Elvin and Elvin [9], Kong et al. [29], and Yang and Tang [64] who formerly used Euler–Bernoulli type Rayleigh–Ritz and finite-element models in conjunction with SPICE (Simulation Program with Integrated Circuit Emphasis) and other circuit simulation software in order to investigate the complete dynamics of the system with a reduced-order energy harvester model in the presence of a nonlinear storage circuit (rather than a linear resistive load). The concept of solving generalized energy harvesting problems with nonlinear circuit components (e.g., diodes) is therefore extended to all three beam theories covered herein.

8.2. Modal decoupling of the governing equations with an example for the Timoshenko model

The aforementioned concept is demonstrated with an example by focusing on a unimorph cantilever modeled based on the Timoshenko beam theory. Recall that the governing dynamics in the presence of a linear resistive load are due to Eqs. (46)–(49), where coupling exists between the mechanical generalized coordinates. Before the system can be represented as a multi-mode transformer,

the coupling between the mechanical generalized coordinates should be eliminated.

Eqs. (46)–(49) can be combined to give

$$\bar{\mathbf{m}}\ddot{\mathbf{p}} + \bar{\mathbf{d}}\dot{\mathbf{p}} + \bar{\mathbf{k}}\mathbf{p} - \bar{\theta}v = \bar{\mathbf{f}}, \quad C_p\dot{v} + \frac{v}{R_l} + \bar{\theta}^t\dot{\mathbf{p}} = 0 \tag{102}$$

where

$$\bar{\mathbf{m}} = \begin{bmatrix} \mathbf{m^{aa}} & \mathbf{0} & \mathbf{0} \\ \mathbf{0} & \mathbf{m^{bb}} & -\mathbf{m^{bc}} \\ \mathbf{0} & -\mathbf{m^{bc}} & \mathbf{m^{cc}} \end{bmatrix}, \quad \bar{\mathbf{d}} = \begin{bmatrix} \mathbf{d^{aa}} & \mathbf{0} & -\mathbf{d^{ac}} \\ \mathbf{0} & \mathbf{d^{bb}} & -\mathbf{d^{bc}} \\ -\mathbf{d^{ac}} & -\mathbf{d^{bc}} & \mathbf{d^{cc}} \end{bmatrix},$$

$$\bar{\mathbf{k}} = \begin{bmatrix} \mathbf{k^{aa}} & \mathbf{0} & -\mathbf{k^{ac}} \\ \mathbf{0} & \mathbf{k^{bb}} & -\mathbf{k^{bc}} \\ -\mathbf{k^{ac}} & -\mathbf{k^{bc}} & \mathbf{k^{cc}} \end{bmatrix} \quad \mathbf{p} = \begin{Bmatrix} \mathbf{a} \\ \mathbf{b} \\ \mathbf{c} \end{Bmatrix}, \quad \bar{\theta} = \begin{Bmatrix} \mathbf{0} \\ -\theta^b \\ \theta^c \end{Bmatrix}, \quad \bar{\mathbf{f}} = \begin{Bmatrix} \mathbf{f} \\ \mathbf{0} \\ \mathbf{0} \end{Bmatrix} \tag{103}$$

Here, the matrices and the vectors have the dimensions of $3N \times 3N$ and $3N \times 1$, respectively. The reason for having $3N$ here as the total dimension is merely because the same number of modes (N) was assumed for each independent mechanical generalized coordinate at the beginning with Eq. (45).

Since the mass and stiffness matrices are symmetric and positive definite [33] and the system is forced to be a normal-mode system [65] due to assuming proportional damping in Eq. (62), one can focus on the eigenvalue problem of the undamped homogeneous system in short-circuit ($R_l \to 0$, hence $v \to 0$) conditions:

$$(\bar{\mathbf{k}} - \chi\bar{\mathbf{m}})\hat{\mathbf{p}} = \mathbf{0} \tag{104}$$

where the eigenvalues (χ_r) are related to the undamped short-circuit natural frequencies (ω_r) through $\chi_r = \omega_r^2$, $r = 1, \ldots, 3N$. The $3N \times 1$ eigenvectors are then normalized with respect to the mass matrix ($\hat{\mathbf{p}}_r^t\bar{\mathbf{m}}\hat{\mathbf{p}}_r = 1$ for more r) for convenience and the following mass-normalized modal matrix is constructed:

$$\mathbf{\Lambda} = \begin{bmatrix} \hat{\mathbf{p}}_1 & \hat{\mathbf{p}}_2 & \ldots & \hat{\mathbf{p}}_{3N} \end{bmatrix} \tag{105}$$

Following Meirovitch [33], the coordinate transformation that can be used for decoupling the mechanical generalized coordinates is

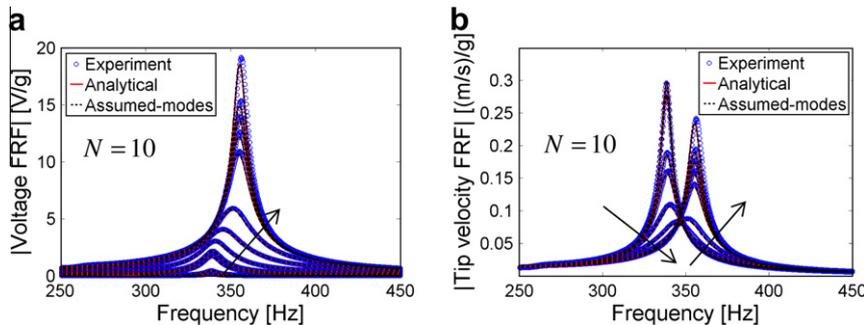$$\mathbf{p} = \mathbf{\Lambda}\mathbf{s} \tag{106}$$

Fig. 10. Comparison of the (a) voltage FRFs and (b) tip velocity FRFs against the experimental data and the analytical solution in the presence of a tip mass ($N = 10$ in the assumed-modes solution and the arrows indicate the direction of increasing load resistance).

Table 5
Assumed-modes predictions of the fundamental short-circuit and open-circuit resonance frequencies of the voltage FRF in the presence of a tip mass (compared against the analytical and the experimental results).

	Short-circuit resonance frequency [Hz]	Open-circuit resonance frequency [Hz]
Experimental	338.4	356.3
Analytical	338.5	355.4
Assumed-modes (N = 1)	344.6	365.3
Assumed-modes (N = 3)	338.7	355.8
Assumed-modes (N = 5)	338.5	355.5
Assumed-modes (N = 10)	338.5	355.4

Substituting Eq. (106) into Eqs. (102), and then pre-multiplying the first one of Eqs. (102) by $\mathbf{\Lambda}^t$ leads to

$$\hat{\mathbf{m}}\ddot{\mathbf{s}} + \hat{\mathbf{d}}\dot{\mathbf{s}} + \hat{\mathbf{k}}\mathbf{s} - \hat{\theta}v = \hat{\mathbf{f}}, \quad C_p\dot{v} + \frac{v}{R_l} + \hat{\theta}^t\dot{\mathbf{s}} = 0 \tag{107}$$

where

$$\hat{\mathbf{m}} = \mathbf{\Lambda}^t\bar{\mathbf{m}}\mathbf{\Lambda} = \mathbf{I}, \quad \hat{\mathbf{d}} = \mathbf{\Lambda}^t\bar{\mathbf{d}}\mathbf{\Lambda}, \quad \hat{\mathbf{k}} = \mathbf{\Lambda}^t\bar{\mathbf{k}}\mathbf{\Lambda}, \quad \hat{\theta} = \mathbf{\Lambda}^t\bar{\theta},$$
$$\hat{\mathbf{f}} = \mathbf{\Lambda}^t\mathbf{f} \tag{108}$$

Here, $\mathbf{I}$ is the identity matrix while the components of the diagonal matrices are

$$\hat{\mathbf{m}} = \text{diag}(m_{11}, m_{22}, \ldots, m_{3N3N}), \quad \hat{\mathbf{d}} = \text{diag}(d_{11}, d_{22}, \ldots, d_{3N3N}),$$
$$\hat{\mathbf{k}} = \text{diag}(k_{11}, k_{22}, \ldots, k_{3N3N}) \tag{109}$$

The advantage of mass-normalization ($\hat{\mathbf{p}}_r^t\bar{\mathbf{m}}\hat{p}_r = 1$) of the eigenvectors is that the diagonal elements in Eqs. (109) are $m_{rr} = 1$, $d_{rr} = 2\zeta_r\omega_r$, and $k_{rr} = \omega_r^2 (r = 1, \ldots, 3N)$, where ζ_r is the modal viscous damping ratio (that is often identified experimentally [10,63] and preferably in short-circuit conditions if the standard experimental modal analysis techniques are to be used [66]). Since the coefficient matrices in Eqs. (107) are diagonal, the coupling between the mechanical generalized coordinates is eliminated in the transformed coordinates denoted by $\mathbf{s}$.

8.3. Representation of the transformer equations in conjunction with nonlinear circuitry

Following the discussion of the previous section, the generalized power generator – energy storage circuit schematic shown in Fig. 12 is for a unimorph piezoelectric energy harvester based on the Timoshenko model. This schematic consists of the complete representation of power generation (with all vibration modes used in the assumed-modes solution), AC-DC conversion (a full-wave rectifier and a smoothing capacitor), and a DC-DC voltage regulation circuit followed by a storage component (a battery or a capacitor). The nonlinearity in the circuit starts with diodes of the full-wave rectifier. Such circuits [26–29] include several other nonlinear electronic components and processes, making it necessary to perform time-domain numerical simulations using an appropriate simulator software. The task of the designer for a full system analysis is to take the left-hand-side components of the transformers in Fig. 12 from the assumed-modes solution in order to design and analyze the resulting nonlinear power generation and energy storage circuit.

The importance of the decoupling process summarized in the previous section is that the left-hand-side transformer components (due to the assumed modes) in Fig. 12 are coupled with the rest of circuit through the transformers only. It is straightforward to notice from Fig. 12 that, if a linear resistor was placed right after the inherent piezoelectric capacitance (C_p) instead of the nonlinear circuit, the schematic would belong to the linear AC problem governed by Eq. (102). In the present schematic shown in Fig. 12, a constant DC signal is obtained after the smoothing capacitor (C_{rect}). Often a DC-DC converter (step-up or step-down) is used since the direct voltage output right after the smoothing capacitor (which is a function of the vibration input) does not necessarily match the voltage level of the storage component [28] nor does the direct output after the rectifier ensure the optimal power transfer to the external load. DC-DC converters are often designed to maximize the power transfer by optimizing their duty cycle [26–29]. Several other nonlinear circuit topologies exist for the maximum power transfer and performance enhancement as recently reviewed by Szarka et al. [67], which can be combined with the transformer components taken from the unimorph and bimorph assumed-modes solutions (based on the Euler–Bernoulli, Rayleigh, or Timoshenko beam
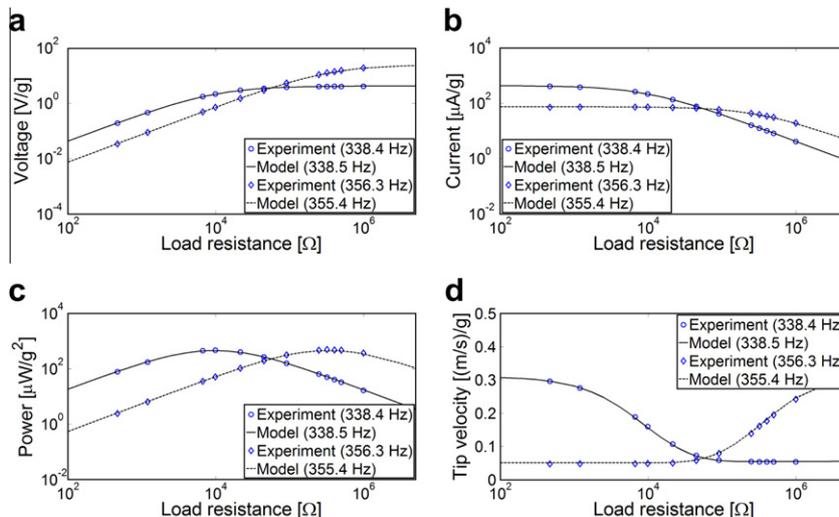

Fig. 11. Variations of the (a) voltage, (b) current, (c) power, and (d) tip velocity amplitudes (per base acceleration input) with changing load resistance for excitations at the fundamental short-circuit and open-circuit resonance frequencies in the presence of a tip mass (N = 10).
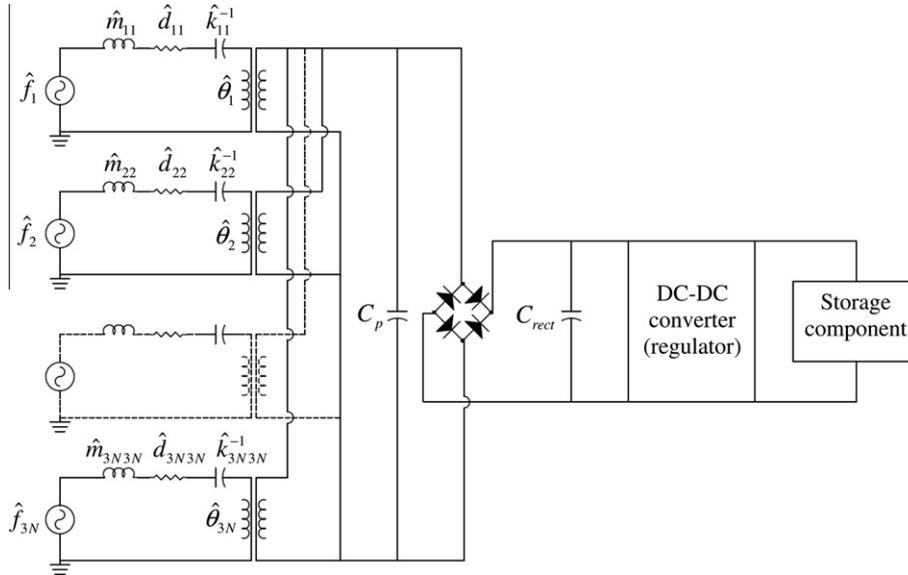
Fig. 12. Schematic of a unimorph piezoelectric energy harvesting and storage system based on the Timoshenko model of the cantilever as components on the left-hand-side of the transformers for each assumed mode in decoupled generalized coordinates, an AC–DC converter (full-wave rectifier with a smoothing capacitor), a DC–DC converter, and a storage component.

models) for a complete analysis of the power generation and energy storage problem.

9. Conclusions

Approximate analytical distributed-parameter modeling of cantilevered piezoelectric energy harvesters is presented in this paper based on different beam theories. An electromechanical version of the assumed-modes method of structural dynamics is used to discretize the energy equations into electromechanical Lagrange's equations derived from the extended Hamilton's principle. The derivations are given based on the Euler–Bernoulli, Rayleigh, and Timoshenko beam theories. In all cases, an axial displacement variable is defined to capture its coupling with the transverse displacement or the cross-section rotation due to unsymmetric laminates. In order to demonstrate modeling of an unsymmetric configuration, the focus is placed on a unimorph energy harvester. Simplification of the governing equations for symmetric bimorph configurations is also shown and the effect of a tip mass on the resulting formulation is discussed. A short discussion regarding the kinematically admissible functions to be used in the models derived here is also provided. Experimental case studies are given for a thin bimorph cantilever to validate the assumed-modes solution using different number of admissible trigonometric functions in the absence and presence of a tip mass. The predictions of the assumed-modes solution are also compared with the analytical solution and excellent agreement is observed. Finally, modal decoupling of the governing electromechanical equations is discussed to establish a multi-mode transformer representation so that the assumed-modes solution can be combined with nonlinear energy harvesting and storage circuits for time-domain simulations. The derivations given in this paper can be used for predicting the electromechanical response of moderately thick cantilevers as well as cantilevers with unsymmetric laminates and varying cross-section. For piezoelectric energy harvester configurations with larger thickness and further pronounced transverse shear distortion effects, higher-order shear deformable theories [69–72] can be employed in a similar fashion for improved accuracy and to eliminate the need for a shear correction factor.

Appendix A. Constitutive equations for one-dimensional bending of a poled narrow piezoceramic layer

A.1. Euler–Bernoulli and Rayleigh models

For one dimensional bending based on the Euler–Bernoulli and Rayleigh beam theories, the only non-zero stress component is T_1 (axial stress in the x_1-direction), i.e., $T_2 = T_3 = T_4 = T_5 = T_6 = 0$ in the three-dimensional constitutive equations [68]. Along with this simplification, if an electrode pair covers the faces perpendicular to the x_3-direction, $E_1 = E_2 = 0$, yielding

$$\left\{ \begin{array}{c} T_1 \\ D_3 \end{array} \right\} = \left[\begin{array}{cc} \bar{c}_{11}^E & -\bar{e}_{31} \\ \bar{e}_{31} & \bar{\varepsilon}_{33}^S \end{array} \right] \left\{ \begin{array}{c} S_1 \\ E_3 \end{array} \right\} \tag{A.1}$$

where

$$\bar{c}_{11}^E = \frac{1}{s_{11}^E}, \quad \bar{e}_{31} = \frac{d_{31}}{s_{11}^E}, \quad \bar{\varepsilon}_{33}^S = \varepsilon_{33}^T - \frac{d_{31}^2}{s_{11}^E} \tag{A.2}$$

Here, s_{11}^E is the elastic compliance at constant electric field, d_{31} is the piezoelectric strain constant, and ε_{33}^T is the permittivity component at constant stress.

A.2. Timoshenko model

In the Timoshenko beam theory, the non-zero stress components are T_1 (the stress component in the axial direction) and T_5 (the transverse shear stress) so that $T_2 = T_3 = T_4 = T_6 = 0$ in the three-dimensional constitutive equations [68]. Applying also the electric field reduction, $E_1 = E_2 = 0$, one obtains

$$\left\{ \begin{array}{c} T_1 \\ T_5 \\ D_3 \end{array} \right\} = \left[\begin{array}{ccc} \bar{c}_{11}^E & 0 & -\bar{e}_{31} \\ 0 & \bar{c}_{55}^E & 0 \\ \bar{e}_{31} & 0 & \bar{\varepsilon}_{33}^S \end{array} \right] \left\{ \begin{array}{c} S_1 \\ S_5 \\ E_3 \end{array} \right\} \tag{A.3}$$

where

$$\bar{c}_{11}^E = \frac{1}{s_{11}^E}, \quad \bar{c}_{55}^E = \frac{1}{s_{55}^E}, \quad \bar{e}_{31} = \frac{d_{31}}{s_{11}^E}, \quad \bar{\varepsilon}_{33}^S = \varepsilon_{33}^T - \frac{d_{31}^2}{s_{11}^E} \tag{A.4}$$

Note that the transverse shear stress in Eq. (A.3) is corrected due to

$$T_5 = \kappa \bar{c}_{55}^E S_5 \qquad (A.5)$$

where κ is the shear correction factor [42–52].

References

[1] Glynne-Jones P, Tudor MJ, Beeby SP, White NM. An electromagnetic, vibration-powered generator for intelligent sensor systems. Sensor Actuat A 2004;110:344–9.
[2] Mann BP, Sims ND. Energy harvesting from the nonlinear oscillations of magnetic levitation. J Sound Vib 2009;319:515–30.
[3] Daqaq MF. Response of uni-modal duffing-type harvesters to random forced excitations. J Sound Vib 2010;329:3621–31.
[4] Mitcheson P, Miao P, Start B, Yeatman E, Holmes A, Green T. MEMS electrostatic micro-power generator for low frequency operation. Sensor Actuat A 2004;115:523–9.
[5] Chiu Y, Tseng VFG. A capacitive vibration-to-electricity converter with integrated mechanical switches. J Micromech Microeng 2008;20:125009.
[6] Nguyen DS, Halvorsen E, Jensen GU, Vogl A. Fabrication and characterization of a wideband MEMS energy harvester utilizing nonlinear springs. J Micromech Microeng 2010;20:125009.
[7] Roundy S, Wright PK. A piezoelectric vibration based generator for wireless electronics. Smart Mater Struct 2004;13:1131–44.
[8] duToit NE, Wardle BL, Kim S. Design considerations for MEMS-scale piezoelectric mechanical vibration energy harvesters. J Integrated Ferroelectrics 2005;71:121–60.
[9] Elvin NG, Elvin AA. A general equivalent circuit model for piezoelectric generators. J Intell Mater Syst Struct 2009;20:3–9.
[10] Erturk A, Inman DJ. An experimentally validated bimorph cantilever model for piezoelectric energy harvesting from base excitations. Smart Mater Struct 2009;18:025009.
[11] Sodano H, Park G, Inman DJ. A review of power harvesting from vibration using piezoelectric materials. Shock Vib Digest 2004;36:197–205.
[12] Anton SR, Sodano HA. A review of power harvesting using piezoelectric materials (2003–2006). Smart Mater Struct 2007;16:R1–R21.
[13] Priya S. Advances in energy harvesting using low profile piezoelectric transducers. J. Electroceram. 2007;19:167–84.
[14] Cook-Chennault KA, Thambi N, Sastry AM. Powering MEMS portable devices – a review of non-regenerative and regenerative power supply systems with emphasis on piezoelectric energy harvesting systems. Smart Mater Struct 2008;17:043001.
[15] Jeon YB, Sood R, Jeong JH, Kim S. MEMS power generator with transverse mode thin film PZT. Sensor Actuat A 2005;122:16–22.
[16] Choi WJ, Jeon Y, Jeong JH, Sood R, Kim SG. Energy harvesting MEMS device based on thin film piezoelectric cantilevers. J Electroceram 2006;17:543–8.
[17] Erturk A. Piezoelectric energy harvesting for civil infrastructure system applications: moving loads and surface strain fluctuations. J Intell Mater Syst Struct 2011;22:1958–72.
[18] Kim HW, Batra A, Priya S, Uchino K, Markley D, Newnham RE, et al. Energy harvesting using a piezoelectric 'Cymbal' transducer in dynamic environment. Jpn J Appl Phys 2004;43:6178–83.
[19] Feenstra J, Granstrom J, Sodano H. Energy harvesting through a backpack employing a mechanically amplified piezoelectric stack. Mech Syst Signal Process 2009;22:721–34.
[20] Smits JG, Choi W. The constituent equations of piezoelectric heterogeneous bimorphs. IEEE Trans Ultrasonics Ferroelectrics Frequency Control 1991;38:256–70.
[21] Hagood NW, von Flotow A. Damping of structural vibrations with piezoelectric materials and passive electrical networks. J Sound Vib 1991;146:243–68.
[22] Lesieutre GA. Vibration damping and control using shunted piezoelectric materials. Shock Vib Digest 1998;30:187–95.
[23] Hagood NW, Chung WH, von Flotow A. Modelling of piezoelectric actuator dynamics for active structural control. J Intell Mater Syst Struct 1990;1:327–54.
[24] Baz A, Ro J. Vibration control of plates with active constrained layer damping. Smart Mater Struct 1994;5:272–80.
[25] Lesieutre GA, Ottman GK, Hofmann HF. Damping as a result of piezoelectric energy harvesting. J Sound Vib 2004;269:991–1001.
[26] Ottman GK, Hofmann HF, Bhatt AC, Lesieutre GA. Adaptive piezoelectric energy harvesting circuit for wireless remote power supply. IEEE Trans Power Electron 2002;17:669–76.
[27] Ottman GK, Hofmann HF, Lesieutre GA. Optimized piezoelectric energy harvesting circuit using step-down converter in discontinuous conduction mode. IEEE Trans Power Electron 2003;18:696–703.
[28] Guan MJ, Liao WH. On the efficiencies of piezoelectric energy harvesting circuits towards storage device voltages. Smart Mater Struct 2007;16:498–505.
[29] Kong N, Ha DS, Erturk A, Inman DJ. Resistive impedance matching circuit for piezoelectric energy harvesting. J Intell Mater Syst Struct 2010;21:1293–302.
[30] Anton SR, Erturk A, Inman DJ. Multifunctional self-charging structures using piezoceramics and thin-film batteries. Smart Mater Struct 2010;19:115021.
[31] Anton SR, Erturk A, Inman DJ. Multifunctional unmanned aerial vehicle wing spar for low-power generation and storage. AIAA Journal of Aircraft 2012;49:292–301.
[32] Timoshenko S, Young DH, Weaver W. Vibration problems in engineering. New York: John Wiley and Sons; 1974.
[33] Meirovitch L. Fundamentals of vibrations. New York: McGraw Hill; 2001.
[34] Reddy JN. Mechanics of laminated composite plates and shells: theory and analysis. Boca Raton, FL: CRC Press; 2004.
[35] Han SM, Benaroya HB, Wei T. Dynamics of transversely vibrating beams using four engineering theories. J Sound Vib 1999;225:935–88.
[36] Kausel E. Nonclassical modes of unrestrained shear beams. ASCE J Eng Mech 2002;128:663–7.
[37] Stanton SC, Erturk A, Mann BP, Inman DJ. Nonlinear piezoelectricity in electroelastic energy harvesters: modeling and experimental identification. J Appl Phys 2010;108:074903.
[38] Stanton SC, Erturk A, Mann BP, Inman DJ. Resonant manifestation of intrinsic nonlinearity within electroelastic micropower generators. Appl Phys Lett 2010;97:254101.
[39] Dym CL, Shames IH. Solid mechanics: a variational approach. New York: McGraw–Hill; 1973.
[40] Crandall SH, Karnopp DC, Kurtz Jr EF, Pridmore-Brown DC. Dynamics of mechanical and electromechanical systems. New York: McGraw-Hill; 1968.
[41] Strutt JW. The theory of sound. Company, London, UK: MacMillan; 1894. Lord Rayleigh.
[42] Timoshenko SP. On the correction for shear of the differential equation for transverse vibrations of prismatic bars. Philos Mag 1921;41:744–6.
[43] Timoshenko SP. On the transverse vibrations of bars of uniform cross-section. Philos Mag 1922;43:125–31.
[44] Mindlin RD. Thickness-shear and flexural vibrations of crystal plates. J Appl Phys 1951;22:316–23.
[45] Mindlin RD. Forced thickness-shear and flexural vibrations of piezoelectric crystal plates. J Appl Phys 1952;23:83–8.
[46] Cowper GR. The shear coefficient in Timoshenko beam theory. ASME J Appl Mech 1966;33:335–40.
[47] Kaneko T. On Timoshenko's correction for shear in vibrating beams. J Phys D 1975;8:1927–36.
[48] Stephen NG. On the variation of Timoshenko's shear coefficient with frequency. ASME J Appl Mech 1978;45:695–7.
[49] Stephen NG. Timoshenko's shear coefficient from a beam subjected to gravity loading. ASME J Appl Mech 1980;47:121–7.
[50] Hutchinson JR. Shear coefficients for Timoshenko beam theory. ASME J Appl Mech 2001;68:87–92.
[51] Stephen NG, Hutchinson JR. Discussion: shear coefficients for Timoshenko beam theory. ASME J Appl Mech 2001;68:959–61.
[52] Puchegger S, Bauer S, Loidl D, Kromp K, Peterlik H. Experimental validation of the shear correction factor. J Sound Vib 2003;261:177–84.
[53] Kim M, Hoegen M, Dugundji J, Wardle BL. Modeling and experimental verification of proof mass effects on vibration energy harvester performance. Smart Mater Struct 2010;19:045023.
[54] Kim JE, Kim YY. Analysis of piezoelectric energy harvesters of a moderate aspect ratio with a distributed tip mass. ASME J Vib Acoust 2011;133:041010.
[55] Meriam JL, Kraige LG. Engineering mechanics: dynamics. New York: John Wiley and Sons; 2001.
[56] Den Hartog JP. Mechanical vibrations. New York: McGraw-Hill; 1956.
[57] Erturk A, Inman DJ. On mechanical modeling of cantilevered piezoelectric vibration energy harvesters. J Intell Mater Syst Struct 2008;19:1311–25.
[58] Lee J, Schultz WW. Eigenvalue analysis of Timoshenko beams and axisymmetric Mindlin plates by the pseudospectral method. J Sound Vib 2004;269:609–21.
[59] Zhou D, Cheung YK. Vibrations of tapered Timoshenko beams in terms of static Timoshenko beam functions. ASME J Appl Mech 2001;68:596–602.
[60] Roundy S, Wright PK, Rabaey JM. A study of low level vibrations as a power source for wireless sensor nodes. Comput Commun 2003;26:1131–44.
[61] Engineering Fundamentals, Inc. (<http://www.efunda.com/materials/piezo/material_data>).
[62] Shu YC, Lien IC. Analysis of power outputs for piezoelectric energy harvesting systems. Smart Mater Struct 2006;15:1499–502.
[63] Erturk A, Inman DJ. Parameter identification and optimization in piezoelectric energy harvesting: analytical relations, asymptotic analyses, and experimental validations. IMechE J Syst Control Eng 2011;225:485–96.
[64] Yang Y, Tang L. Equivalent circuit modeling of piezoelectric energy harvesters. J Intell Mater Syst Struct 2009;20:2223–35.
[65] Caughey TK, O'Kelly MEJ. Classical normal modes in damped linear dynamic systems. ASME J Appl Mech 1965;32:583–8.
[66] Ewins DJ. Modal testing: theory, practice and application. Baldock, Hertfordshire, UK: Research Studies Press; 2000.
[67] Szarka G, Stark B, Burrow S. Review of power conditioning for kinetic energy harvesting systems. IEEE Trans Power Electron 2011;27:803–15.
[68] Standards Committee of the IEEE Ultrasonics, Ferroelectrics, and Frequency Control Society, 1987, IEEE Standard on Piezoelectricity, IEEE, New York.
[69] Levinson M. A new rectangular beam theory. J Sound Vib 1981;74:81–7.
[70] Reddy JN. A simple higher-order theory for laminated composite plates. ASME J Appl Mech 1984;51:745–52.
[71] Carrera E, Giunta G, Petrolo M. Beam structures: classical and advanced theories. Wiley; 2011.
[72] Carrera E, Petrolo M. On the effectiveness of higher-order terms in refined beam theories. J Appl Mech 2011;78:021013.